



Systematic *in vitro* and *in vivo* study on biodegradable binary Zn-0.2 at% Rare Earth alloys (Zn-RE: Sc, Y, La–Nd, Sm–Lu)

Shaokang Du^a, Yunong Shen^b, Yufeng Zheng^b, Yan Cheng^a, Xiaoxue Xu^{c,*}, Dafu Chen^{d,**}, Dandan Xia^{e,***}

^a Academy for Advanced Interdisciplinary Studies, Peking University, Beijing, 100871, China

^b School of Materials Science and Engineering, Peking University, Beijing, 100871, China

^c School of Biomedical Engineering, Faculty of Engineering and Information Technology, University of Technology Sydney, NSW, 2007, Australia

^d Laboratory of Bone Tissue Engineering, Beijing Laboratory of Biomedical Materials, Beijing Research Institute of Traumatology and Orthopaedics, Beijing Jishuitan Hospital, Beijing, 100035, China

^e Department of Dental Materials, Peking University School and Hospital of Stomatology & National Center of Stomatology & National Clinical Research Center for Oral Diseases & National Engineering Research Center of Oral Biomaterials and Digital Medical Devices & Beijing Key Laboratory of Digital Stomatology & Research Center of Engineering and Technology for Computerized Dentistry Ministry of Health & NMPA Key Laboratory for Dental Materials, Beijing 100081, China

ARTICLE INFO

Keywords:

Biodegradable metals
Zn-Rare Earth alloys
Mechanical property
Biodegradation behavior
Biocompatibility

ABSTRACT

Biomedical implants and devices for tissue engineering in clinics, mainly made of polymers and stiff metallic materials, require possibly secondary surgery or life-long medicine. Biodegradable metals for biomedical implants and devices exhibit huge potential to improve the prognosis of patients. In this work, we developed a new type of biodegradable binary zinc (Zn) alloys with 16 rare earth elements (REEs) including Sc, Y, La to Nd, and Sm to Lu, respectively. The effects of REEs on the alloy microstructure, mechanical properties, corrosion behavior and *in vitro* and *in vivo* biocompatibility of Zn were systematically investigated using pure Zn as control. All Zn-RE alloys generally exhibited improved mechanical properties, and biocompatibilities compared to pure Zn, especially the tensile strength and ductility of Zn-RE alloys were dramatically enhanced. Among the Zn-RE alloys, different REEs presented enhancement effects at varied extent. Y, Ho and Lu were the three elements displaying greatest improvements in majority of alloys properties, while Eu, Gd and Dy exhibited least improvement. Furthermore, the Zn-RE alloys were comparable with other Zn alloys and also exhibited superior properties to Mg-RE alloys. The *in vivo* experiment using Zn–La, Zn–Ce, and Zn–Nd alloys as tibia bone implants in rabbit demonstrated the excellent tissue biocompatibility and much more obvious osseointegration than the pure Zn control group. This work presented the significant potential of the developed Zn-RE binary alloys as novel degradable metal for biomedical implants and devices.

1. Introduction

Biomedical implants and devices for tissue engineering and cardiovascular diseases are under vigorously ongoing research. Biodegradable metals (BMs) exhibit huge potential for biodegradable implants and devices to improve prognostic quality of patients and to assist clinicians as well. BMs possess bio-adaptable mechanical supports, degradation rates, proactive interactions with biological tissues and controllable biocompatible risks compared to biodegradable polymers [1]. Two

criteria for BMs, biocompatibility and biodegradability [2], enables the current development of three main types of BMs, Fe, Mg, and Zn in the pure metal and their alloys. Fe-based BMs exhibit high mechanical strength but very low degradation rate at the range of 50–160 $\mu\text{m}/\text{year}$, which is not suitable in cardiovascular or osteogenic disease healing time. It is also found that the corrosion products from Fe-based BMs cannot be fully metabolized, resulting in inflammatory responses [3,4]. On the contrast, Mg-based BMs displays obvious advantages in biocompatibility, but very high degradation rate in biological

Peer review under responsibility of KeAi Communications Co., Ltd.

* Corresponding author.

** Corresponding author.

*** Corresponding author.

E-mail addresses: xiaoxuehelen.xu@uts.edu.au (X. Xu), chendafugo@aliyun.com (D. Chen), dandanxia@pku.edu.cn (D. Xia).

<https://doi.org/10.1016/j.bioactmat.2023.01.004>

Received 16 November 2022; Received in revised form 3 January 2023; Accepted 3 January 2023

2452-199X/© 2023 The Authors. Publishing services by Elsevier B.V. on behalf of KeAi Communications Co. Ltd. This is an open access article under the CC BY-NC-ND license (<http://creativecommons.org/licenses/by-nc-nd/4.0/>).

environments ($>300 \mu\text{m}/\text{year}$) [5–7], which is too fast to meet the requirements of bone healing cycle [8,9]. In addition, hydrogen gas generated during Mg-based alloys degradation could result in risks of local edema, affecting the healing process [10].

Zn-based BMs is an emerging BM that are more suitable for biomedical implants. The standard electrode potential of Zn (-0.76 V) is between Mg (-2.37 V) and Fe (-0.44 V), so that the degradation rates of Zn-based BMs would be more appropriate to match the biological tissues regeneration process than Fe- and Mg-based BMs. Other than proper degradation rate, the degradation products of Zn-based BMs formed gradually are completely biocompatible and could be metabolized by adjacent biological organism [11]. Moreover, the released Zn^{2+} from degradation is an essential component of a variety of genes and functional proteins, especially, Zn^{2+} is actively involved in bone metabolism. *In vitro* cellular work [12] demonstrated that the low concentration of Zn^{2+} promoted survival, proliferation, adhesion and migration of the primary human Coronary artery cells (HCECs). *In vivo* animal experiments further proved that Zn-based BMs enhanced bone integration ability [13,14]. However, it was pointed out that the positive effects of Zn^{2+} on osteoblast activity occur over a narrow dose range ($1\text{--}50 \mu\text{M}$). Higher doses of Zn^{2+} would inhibit osteogenic activity while lower range than $1 \mu\text{M}$ has no measurable effects [15]. Therefore, developing Zn-based BMs to optimize the degradation rates and monitor the released Zn^{2+} is essential for Zn-based biodegradable implants.

The mechanical supporting role is another very important factor for biodegradable implants, especially, the mechanical integrity of the biomedical implants during the degradation process. The low strength and poor plasticity of pure Zn are required to be improved for load-bearing implants in clinical applications. Alloying other elements is one of the effective means to improve the mechanical properties of metals. In the reported studies, various elements have been alloyed into pure Zn, including Fe [16,17], Mg [18,19], Ca [20], strontium (Sr) [21, 22], lithium (Li) [23,24], copper (Cu) [25], silver (Ag) [26], and manganese (Mn) [27]. These Zn alloys displayed improved mechanical properties together with tailored degradation rates. $1 \text{ wt}\% \sim 3 \text{ wt}\%$ Mg were alloyed into Zn to fabricate Zn–Mg alloys with both improved strength and biocompatibility. The Zn-1wt% Mg alloy with an enhanced strength of 150 MPa and a biologically acceptable corrosion rate of $80 \mu\text{m}/\text{y}$ was adopted as bone fixation screw [10]. Zn–Mg–X ternary alloys were prepared by alloying a third element for further mechanical strengthening. For example, Zn-0.02Mg-0.02Cu ternary alloy presented the enhanced tensile yield strength (TYS) and ultimate tensile strength (UTS) at 216.29 MPa and 262.25 MPa, respectively. Moreover, with the additional Cu, the alloy did not show no serious inflammatory reaction in subcutaneous embedding [28]. The UTS value of Zn–1Mg-0.1Mn alloy was increased to 299.04 MPa, while the hemocompatibility of Zn–1Mg-0.1Mn was still excellent [29,30]. Recently, the highest UTS has been achieved from 120 MPa to 560 MPa for Zn-6 at% Li and the highest corrosion resistance in modified simulated body fluid was presented from Zn-4at%Li alloy [24]. Ternary Zn–Li alloys, including Zn–Li–Sr alloys and Zn–Li–Ca alloys, showed even higher mechanical strength and much improved biocompatibility and bioactivity. The Zn-0.8Li-0.1Ca alloy reached to 567.60 MPa in UTS and it also greatly stimulated the expression of osteogenesis-related genes (ALP, COL-1, OCN and Runx-2), suggesting the Zn–Li–Ca alloy's potential in regenerative load-bearing bone implants [31]. Zn-0.8Li-0.1Sr exhibited excellent overall mechanical properties with the UTS at 524.33 MPa, and the uniformly slow corrosion [32]. Zn-based BMs have also been exploited for very broad biomedical applications as surgical sutures devices [33]. The ternary and quaternary alloys of Zn-1.0X-0.1Ti (X: Mn, Cu) and Zn-1.0Cu-0.2Mn-0.1Ti alloy designed for surgical staples displayed the significantly enhanced TYS and well-maintained bendability. The *in vivo* implantation experiments in rabbits presented neither complications nor inflammatory reactions in the tissues adjacent to the alloy staples.

REEs are also common alloying elements that have been widely used

in metallurgical industry to enhance the strength of metal [7,34]. REEs have excellent metallurgical effect by settling with impurities, such as Cu, nickel (Ni), Fe, to purify melts in the smelting process [35]. REEs have been adopted in Mg-based BMs, such as Mg–Al–RE alloy, Mg–Y–RE alloy, and Mg–Ag–Nd–Zr alloy [7,36,37]. Liu et al. [38] prepared Mg–RE binary alloys by adding 16 REEs into Mg. Under the same preparation process and experimental conditions, the improving effects of the REEs on the microstructure, mechanical properties, corrosion behavior and biocompatibility of Mg were systematically investigated and analyzed.

However, the research work on Zn–RE alloys are still very rare and scattered. It is mainly attributed to the difficulties for processing such a large group of elements with the optimized alloying amount of the REEs in Zn to estimate their improving effects. Because the solid solubility of REE in Zn is very low at room temperature, to ensure the second phase formation and their uniform distribution in Zn matrix, we alloyed 16 REEs with a very low alloying concentration of 0.2 at% into pure Zn in this study. Except the radioactive element promethium (Pm), the REEs of scandium (Sc), yttrium (Y), and REEs from lanthanum (La) to neodymium (Nd), and samarium (Sm) to lutecium (Lu) were alloyed into the pure Zn and 16 Zn–RE alloys were prepared. We systematically investigated the microstructures, mechanical properties, degradation behaviors and biological responses of all the Zn–RE alloys. We compared these properties of the Zn–RE alloys with the pure Zn and among the 16 Zn–RE alloys. The effects of different REEs on a variety of performances were analyzed. Three Zn–RE alloys were selected for *in vivo* assessments as bone implants. The comprehensive study of this work provides pilot data for new biodegradable Zn-based BMs design as biomedical implants and devices materials.

2. Materials and methods

2.1. Materials preparation and processing

The alloy concentrations of the REEs in Zn was selected as 0.2 at% after we studied the phase diagrams and thermodynamic data of the Zn–RE system. Fig. 1(a) shows the phase diagrams of the binary Zn–RE systems with the preferentially formed intermetallic compounds and their proportions along the atomic percentage of RE in the alloy [39,40]. At room temperature, the solid solubility of all the 16 REEs to alloy in Zn matrix is very low, therefore, the alloyed RE elements would mainly exist in the form of intermetallic compound in the Zn–RE alloys, as listed in Fig. 1(a). These formed second phases could be able to enhance the mechanical properties, however, the amount and distributions of the second phases within Zn matrix is critical for the strengthening mechanism. The other factor determining the REEs concentration is biocompatibility as none of REEs is inherent element in organisms, hence, low concentration of REE would be preferred for the polit studies.

Pure Zn and all Zn–RE alloys were supplied by the Hunan Institute of Rare Earth Materials, China. The designed binary Zn–RE was 0.2 at%RE (RE = Sc, Y, La, Ce, Pr, Nd, Sm, Eu, Gd, Tb, Dy, Ho, Er, Tm, Yb and Lu) as-cast alloys. Since all the RE elements were alloyed with the same 2% atomic concentration, we designate Zn–RE to represent all Zn-0.2 at% RE alloys. The exact compositions, including alloy elements and impurities, were characterized using an Inductively Coupled Plasma Optical Emission Spectrometer (ICP-OES, Agilent Varian 700, USA). The data was collected and showed in Table S1. The as-cast alloys were processed into cylindrical workpieces in the dimensions of $\Phi 39.6 \times 50 \text{ mm}$ using a Wire Electrical Discharge Machining machining firstly and then further processed through the hot-extrusion treatment at $260 \text{ }^\circ\text{C}$ for 2 h with the extrusion rate of $1 \text{ mm}/\text{s}$ and the extrusion ratio of 10. The Zn–RE alloy rods with a diameter of 12 mm were obtained by a single extrusion. The rods were cut into $\Phi 12 \times 2 \text{ mm}$ discs for microstructural textures characterization, biocorrosion test and biocompatibility tests. All samples were sanded with SiC sandpaper to 2000 grit, ultrasonic cleaned with water and ethanol and then dried in the open air.

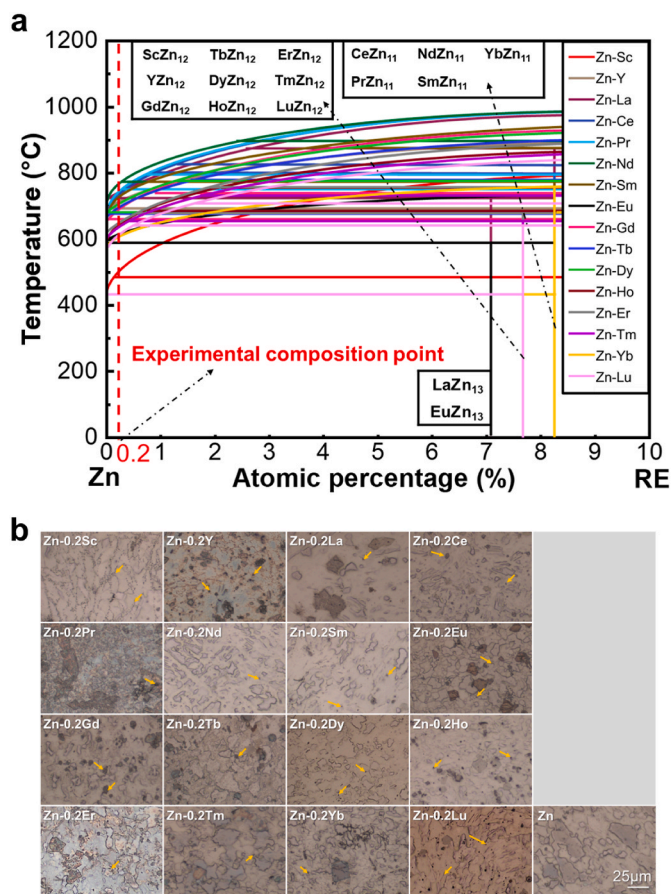


Fig. 1. (a) Summary of phase diagram of the binary Zn-RE alloy. (b) Optical microscope images of microstructures of the pure Zn and binary Zn-RE alloys.

2.2. Microstructure characterization

2.2.1. Metallographic observation

The $\Phi 12 \times 2$ mm disc specimen were ground firstly and then polished with 5000 grit SiC sandpaper, and cleaned with sonication bath in anhydrous ethanol. The discs were then polished with chemical polishing electrolyte (20 mL $C_3H_8O_3$, 2 mL HCl (36.0–38.0%), 3 mL HNO_3 (65.0–68.0%), and 5 mL CH_3COOH). Lastly, the surfaces of the discs were etched using 4% nitric acid aqueous solution. The microstructures of the specimen were observed and imaged using a DMI3000 M metallographic microscope.

2.2.2. X-ray diffraction (XRD) analysis

The sanded discs were used for XRD analysis. The phase compositions of the samples were analyzed with a Rigaku DMAX 2400 X-ray diffractometer with a Cu source ($\lambda = 1.5406 \text{ \AA}$). The scanning range was set to 10° – 90° and the scanning speed was $4^\circ/\text{min}$.

2.3. Mechanical performance test

2.3.1. Tensile test

The rod samples were machined into the standard samples for tensile tests according to the ASTM-E8-04 [41]. Tensile experiments were carried out on an Instron 5969 universal material test machine with a tensile strain rate of 4%/min at room temperature. The UTS, TYS and elongation at break of the alloys were obtained from the tensile tests. The fracture morphology of the alloys was characterized using a scanning electron microscopy (SEM, Hitachi S-4800). Five parallel samples were tested in each group.

2.3.2. Compression test

Cylindrical samples with the dimensions of $\Phi 5 \times 15$ mm were prepared for compression tests according to the ASTM E9-89A (2000) [42]. The compression experiments were carried out on an Instron 5969 universal material test machine with the compression rate of 0.9 mm/min. The ultimate compressive strength (UCS), and the compressive yield strength (CYS) of the alloys were obtained. Five parallel samples were tested in each group.

2.3.3. Microhardness test

Micro-hardness test was performed on the HMV-2T digital microhardness instrument (Shimadzu, Japan). The applied pressure was 980.7 mN, and the pressure was maintained for 15 s. Five parallel samples were tested in each group.

2.4. In vitro degradation test

2.4.1. Electrochemical test

The electrochemical test was conducted according to the ASTM-G102-89 standard [43]. A saturated calomel electrode (SCE) was used as the reference electrode, a platinum plate was used as the auxiliary electrode, and the testing alloy sample was the working electrode. The electrolyte was the simulated body fluid (SBF) with the following formula: NaCl 8.035 g/L, $NaHCO_3$ 0.355 g/L, KCl 0.225 g/L, $K_2HPO_4 \cdot 3H_2O$ 0.231 g/L, $MgCl_2 \cdot 6H_2O$ 0.311 g/L, $CaCl_2$ 0.292 g/L, Na_2SO_4 0.072 g/L, and Tris 6.118 g/L. A Swiss Vantone Electrochemistry Workstation PGSTAT 302 N was used for the electrochemical tests. The open circuit potential curve (OCP) of the alloys in SBF solution were firstly measured for 3600 s. The OCP curves are shown in Fig. S5. Alternative Current (AC) impedance spectra of the alloy samples were measured at the open circuit potential with the spectrum range from 100 kHz to 10 MHz. The potentiodynamic polarization curve was measured from -500 mV(vs. SCE) to 1000 mV(vs. SCE) at a scanning rate of 0.001 V/s.

2.4.2. Immersion test

The immersion experiment was carried out according to ASTM G31-72 standard [44]. The disc samples were ground with 2000 grit SiC sandpaper, cleaned with sonication bath in water and ethanol, dried and weighed before immersed the disc samples into SBF. The ratio of the SBF volume to the sample surface area was $20 \text{ mL}/\text{cm}^2$, and the SBF was kept in a water-bath at 37°C . The disc samples were immersed in SBF for 28 days and then were taken out from the SBF, washed with deionized water and dried in air. A VCAD-1010 precision imaging instrument was used to image the corrosion morphology at macroscopic scale for the corroded samples. The Hitachi S-4800 SEM equipped with the Energy Dispersive X-ray spectroscopy (EDS) was used to observe the corrosion morphology of the samples at microscale, and to analyze the composition of the corrosion products. Lastly, the corrosion products on the disc samples surfaces were removed by sonicating the disc samples in an aqueous solution of CrO_3 (200 g/L). The disc samples were then cleaned with deionized water and anhydrous ethanol. After drying, the sample was weighed and the corrosion rate (CR) was calculated according to the formula $CR = 3.65\Delta W/\rho$. In the equation, ΔW represents the weight loss rate of metal ($\text{mg}/\text{cm}^2/\text{d}$), ρ is the material density. The above steps are performed according to ASTM-G1-90 standards [45]. Four parallel samples were measured for statistical analysis.

2.5. In vitro biocompatibility assessment

2.5.1. Cytotoxicity test

The cell viability of Mouse fibroblasts (L929 cells), Human Umbilical Vein Endothelial Cells (HUVEC) and Mouse embryonic osteoblasts cell (MC3T3-E1 cell) was assessed via an indirect contact method. Dulbecco's modified eagle medium (DMEM) medium was supplemented with 10% fetal bovine serum (FBS) and 1% penicillin - streptomycin for cell culture. After UV sterilization, the disc samples were immersed into the

cell culture medium with the surface area to medium volume ratio of $1.25 \text{ cm}^2/\text{mL}$ for 24 h to obtain the extracts. The concentrations of Zn^{2+} in the obtained extract of each Zn-RE alloy were measured using ICP-OES (Avio 200). Cells were placed in 96-well plates at a density of $5 \times 10^3/100 \mu\text{L}$ and cultured for 24 h. Cells were then cultured with the alloys extracts that were diluted to certain concentrations. Negative control group was the cells cultured in the cell culture medium and positive control group was the cells cultured in a cell culture medium containing 10% dimethyl sulfoxide. The extracts of the pure Zn and Zn-RE alloys were refreshed every two days. Cells after co-cultured with the alloys extracts for 1, 3, and 5 days were counted a Cell Counting Kit-8 (CCK-8). The cytotoxicity of alloy samples was quantitatively assessed by comparing absorbance values of the medium stained with CCK-8 reagent. Each test was repeated three times, with five parallel samples each time.

2.5.2. Hemolysis test

Fresh blood was collected from healthy New Zealand rabbits and then 3.8 wt% sodium citrate was added to the blood samples. The volume ratio of the collected blood to the added sodium citrate was 9:1. Then the blood samples mixed with sodium citrate were diluted using PBS with the volume ratio of the blood to PBS of 4:5. The diluted blood samples were transferred into a centrifuge tube and the tube was immersed into 10 ml PBS at 39°C for 30 min. The equal volume of deionized water and PBS solution were used as the positive control group and the negative control group respectively. The sample was immersed in 10 mL PBS for 30 min, the temperature was kept at 39°C , and then 0.2 ml of blood was added. These mixed solutions were cultured in the alloy extracts at 39°C for 60 min, and then these samples were centrifuged to get the supernatant. The absorbance values of the supernatants at 545 nm were measured by an enzyme-plate analyzer (Bio-RAD 680). Three parallel samples were set for each material.

2.5.3. Blood platelet adhesion test

The fresh blood of New Zealand rabbits was centrifuged at 1000 rpm for 15 min to obtain platelet-rich plasma (PRP) from the supernatant. The discs samples were placed in a 24-well plate, and 0.4 ml PRP was added to each well to ensure that the sample was submerged in the PRP. After 60 min' culture at 39°C , PRP was removed and the discs samples were gently rinsed with PBS for 3 times. Platelets on the disc sample surfaces were fixed using the 2.5% glutaraldehyde solution for 60 min, and then dehydrated in the gradient ethanol solutions (50%, 60%, 70%, 80%, 90%, 100%) for 10 min respectively. Then, the disc samples were dried in a dryer at 25°C . The morphology of the blood platelets on the disc sample surfaces was observed using SEM. The test was repeated three times with five parallel samples each time.

2.6. In vivo implantation

Animal experiment was approved by the Ethics Committee of Peking University Health Science Center, Beijing, China (LA2019019). The surgery was carried out according to the protocol established by the Experimental Animal Ethics branch. Five-month old male New Zealand rabbits were anesthetized with pentobarbital sodium (30 mg/kg) via the ear vein administration to minimize suffering. Bilateral holes (2 mm in diameter and 6 mm in depth) were created in the tibia using a dental drill, and normal saline was used to cool the bone tissue. The cylindrical samples ($\Phi 2 \times 6 \text{ mm}$) of the Zn-La, Zn-Ce and Zn-Nd alloys were placed into the predrilled holes. Finally, the incision was sutured in a layer by layer manner using non-absorbable thread. Five parallel samples of each material were implanted.

After 6- and 12-weeks' implantation, the ear arterial blood sample was collected from each rabbit. Then, the rabbits were sacrificed with overdosed pentobarbital sodium, and the tibia and organs including hearts, livers, spleens, lungs, and kidneys were collected. The metallic ions' concentrations in the blood serum were measured using the ICP-

OES. The tibia and the organs were fixed in 10% buffered formalin for 24 h. The bone tissue samples were observed from the hard tissue section. The tibia was dehydrated with gradient ethanol solutions and embedded in the polymethylmethacrylate resins. The embedded tibia samples were sliced to 200 μm and then ground to 30–40 μm , followed by methylene blue/acid fuchsin staining. After the embedded sections were polished and smoothed using the 5000 grit SiC sandpaper, the interface between the implant and bone tissue was examined using SEM. EDS was used to map the compositions of the bone and the alloy samples at the interface to analyze the corrosion products, to assess the local element metabolism and to observe the diffusion of the implant. The organ tissues were sampled and stained with hematoxylin-eosin staining (HE). Finally, the tissue sections were imaged using an optical microscope (BX53; Olympus, Japan).

2.7. Statistical analysis

The experimental results were expressed as mean \pm standard deviation. One-way analysis of variance (ANOVA) and Tukey test were used to analyze the variance. $P < 0.05$ was considered statistically significant.

3. Results

3.1. Microstructures of the Zn-RE alloys and pure Zn

Fig. 1(a) illustrate the binary Zn-RE phase diagram of experimental REEs (Sc, Y, La, Ce, Pr, Nd, Sm, Eu, Gd, Tb, Dy, Ho, Er, Tm, Yb and Lu). It can be seen the Zn-0.2 at%RE alloys have the dual phase microstructure at room temperature. The secondary phases are REZn_{13} , REZn_{12} and REZn_{11} , respectively. Fig. 1(b) shows the metallographic morphology of Zn-RE alloys and pure Zn using an optical microscope. The microstructures of the Zn-RE alloys varied a lot from the pure Zn and also among each other. The average grain size of the pure Zn is $\sim 19.2 \mu\text{m}$, and the grain sizes of the Zn-RE alloys range from 6.2 to 17 μm . General speaking, the grain size of Zn-RE alloy is relatively smaller than that of pure Zn. In addition, there are elongated deformation of the grains in the alloys of Zn-Sc, Zn-Y, Zn-Ce, Zn-Nd, Zn-Sm, Zn-Ho, and Zn-Lu. The second phases can be observed in each Zn-RE alloy, as labelled using the yellow arrows in the corresponding micrographs. The size and quantity of the second phase are also different. The second phase with relatively small size, high proportion and even distribution is shown in the alloys of Zn-Y, Zn-Ce and Zn-Ho. While large and thick second phases can be found from the alloys of Zn-Sc, Zn-La, Zn-Pr and Zn-Eu, especially, the largest second phase was exhibited in Zn-Pr with deformed shapes and broken pieces from extrusion.

The phase composition of the alloys identified via XRD are shown in Fig. S1. Pure Zn presents the XRD peaks of α -Zn phase with the three dominant crystal planes of (002), (100) and (101). The Zn-RE alloys also mainly exhibit the α -Zn phase with minor presentations of the second phases. The second phases in the Zn-RE alloys can be indexed to the diffraction peaks of the intermetallic compounds REZn_x ($x = 11, 12$ and 13) which are consistent with those compounds preferentially formed in the Phase Diagram shown in Fig. 1(a).

3.2. Mechanical properties

Figs. S2(a) and (b) shows the mechanical tensile and compression stress-strain curves of the Zn-0.2 at%RE alloys. After careful calculation and comparison based on Fig. S2, we summarized the TYS, UTS and uniform elongation (UE, corresponding to the elongation at UTS) of the Zn-RE alloys in Fig. 2(a–c). Comparing to the pure Zn, the TYS, UTS and UE of the Zn-RE alloys are all significantly increased, suggesting both the strength and ductility of the Zn-RE alloys can be enhanced by the addition of REEs into Zn matrix. It is worth noting that among the 16 REEs, alloying Y with Zn exhibits significant improvement in all three tensile properties. The TYS, UTS and UE of Zn-Y alloy is 5.08 times, 3.48

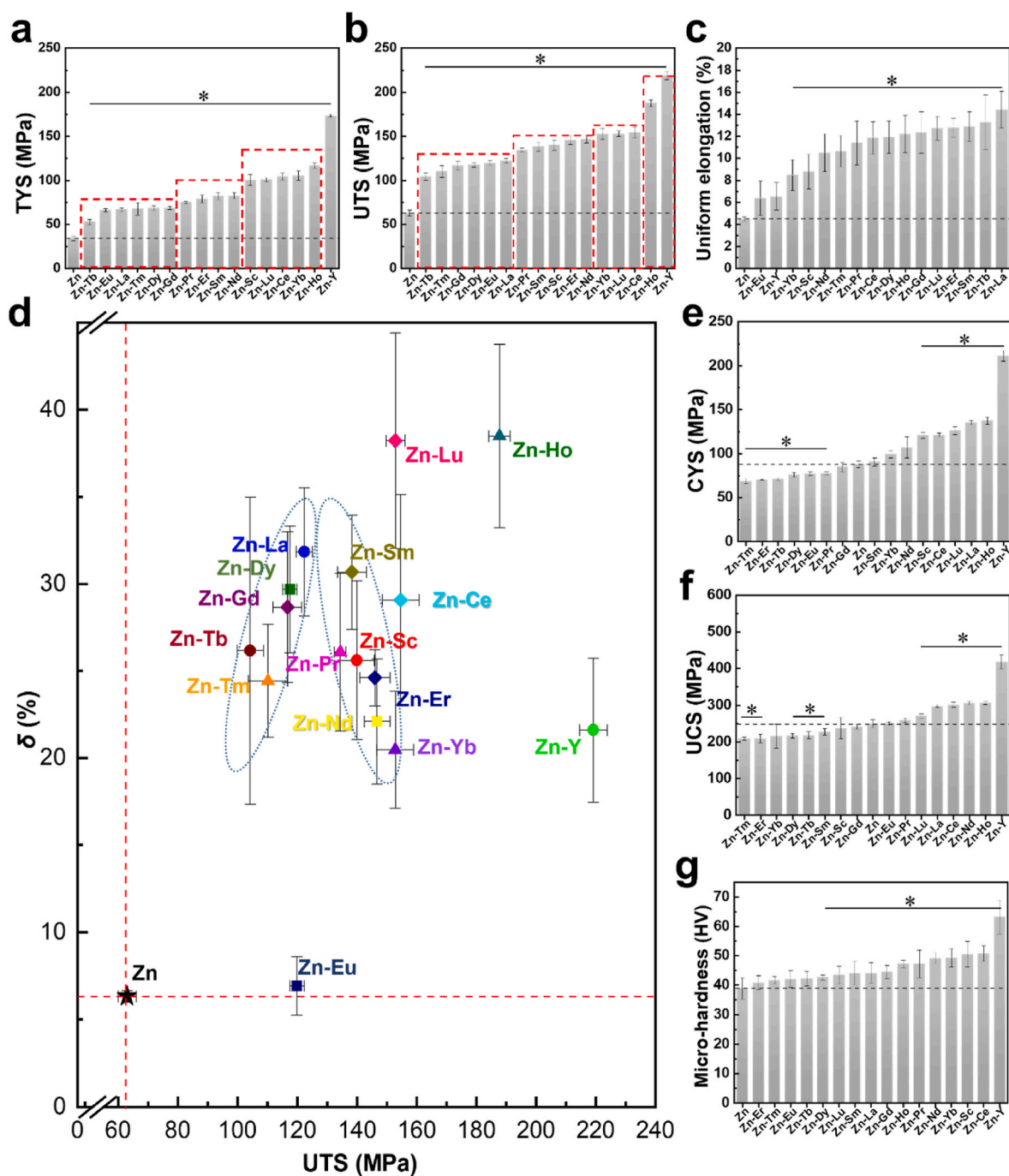


Fig. 2. Mechanical properties of the pure Zn and binary Zn-RE alloys: (a) TYS, (b) UTS, (c) Uniform elongation, (d) The scatter diagram of fracture elongation and UTS. (e) CYS, (f) UCS, and (g) Micro-hardness. Error bars indicate mean \pm standard deviation (tensile, compressive and micro-hardness tests, $n = 5$). * $P < 0.05$ by one-way ANOVA with Tukey’s post hoc test, compared with pure Zn.

times, and 1.45 times higher than that of pure Zn, respectively. The tendency of mechanical improvement effect from the alloyed REEs were categorized into four groups. In term of the TYS and UTS, the group of La, Eu, Gd, Tb, Dy and Tm shows ≤ 2 times enhancement effect on that of the pure Zn, then the group of Pr, Nd, Sm and Er exhibits relative higher enhancement of 2–2.5 times, followed by the group of Sc, Ce, Yb and Lu with further enhancement to 3–3.5 times. Ho and Y are the last two alloy elements with greatest improving effect. In terms of the UE, the above four groups are in a opposite tendency. Y and Eu shows least improvement, followed by the group of Yb and Sc, and the group of Nd and Tm. The group of Ce, Pr and Sm, Gd to Er presents similarly drastic increase in UE and La is the champion element showing greatest UE enhancement

to 14.41%.

Fig. 2(d) summaries the scatter diagram of the fracture elongation (δ) and UTS of pure Zn and Zn-RE alloys. UE represents the degree of uniform deformation of the tensile sample before it bears the ultimate tensile stress, while fracture elongation refers to the degree of elongation of the material when it is broken. The higher the fracture elongation is, the less likely the material is to suddenly fail. Here in the scatter diagram we adopted the fracture elongation values together with the UTS to estimate the strength and ductility of the Zn-RE alloys. It can be seen that alloying 0.2 at% REEs into Zn can significantly improve both the tensile strength and ductility. Although the UTS has been enhanced almost 2 times for Zn–Eu alloy, the elongation is increased slightly, which

presents Zn–Eu on the middle-bottom of the scatter diagram. There are roughly two groups in the scatter diagram presenting two different variation trends between the UTS and elongation of the Zn–RE alloys. At relatively low UTS range (UTS <130 MPa), the elongation moves from low to high while the UTS value of the Zn–Tb, Tm, Gd, Dy and La alloys increases. When UTS >130 MPa and the UTS of the Zn–Pr, Sc, Er, Nd, and Yb alloys increases, the elongation decreases. It also can be found that with the same UTS, the elongation of the Zn–Lu, Ce and Yb alloys varies a lot. The elongation of the Zn–Ho is increased to the same extent with that of Zn–Lu, however, the UTS of Zn–Ho is higher than Zn–Lu. It is clear that the Zn–Y alloy presents highest UTS while the elongation is relatively low. The Zn–RE alloys with the best combination of fracture

elongation and UTS are Zn–Ho, Zn–Lu and Zn–Y.

Fig. 2(e–g) show the CYS, UCS and hardness of the Zn–RE alloys respectively. The addition of each REEs, Sc, Y, La, Ce, Nd, Ho, Yb and Lu, exhibits enhancement on the CYS. The Zn–Y alloy presents highest CYS of 211.25 MPa which is 2.40 times higher than that of the pure Zn. While the rest REEs including Pr, Sm, Eu–Dy, Er, and Tm does not improve the compression performance of pure Zn. The improvement effect of the REEs to the UCS of pure Zn is less obvious compared to the improvement to the CYS of the pure Zn. Only Y, La, Ce, Pr Nd and Ho exhibit enhancement effect to the CYS of the pure Zn and the Zn–Y is still the most outstanding one with the UCS of 417.91 MPa. All REEs increases the hardness after alloyed into Zn matrix and Zn–Y alloy displays

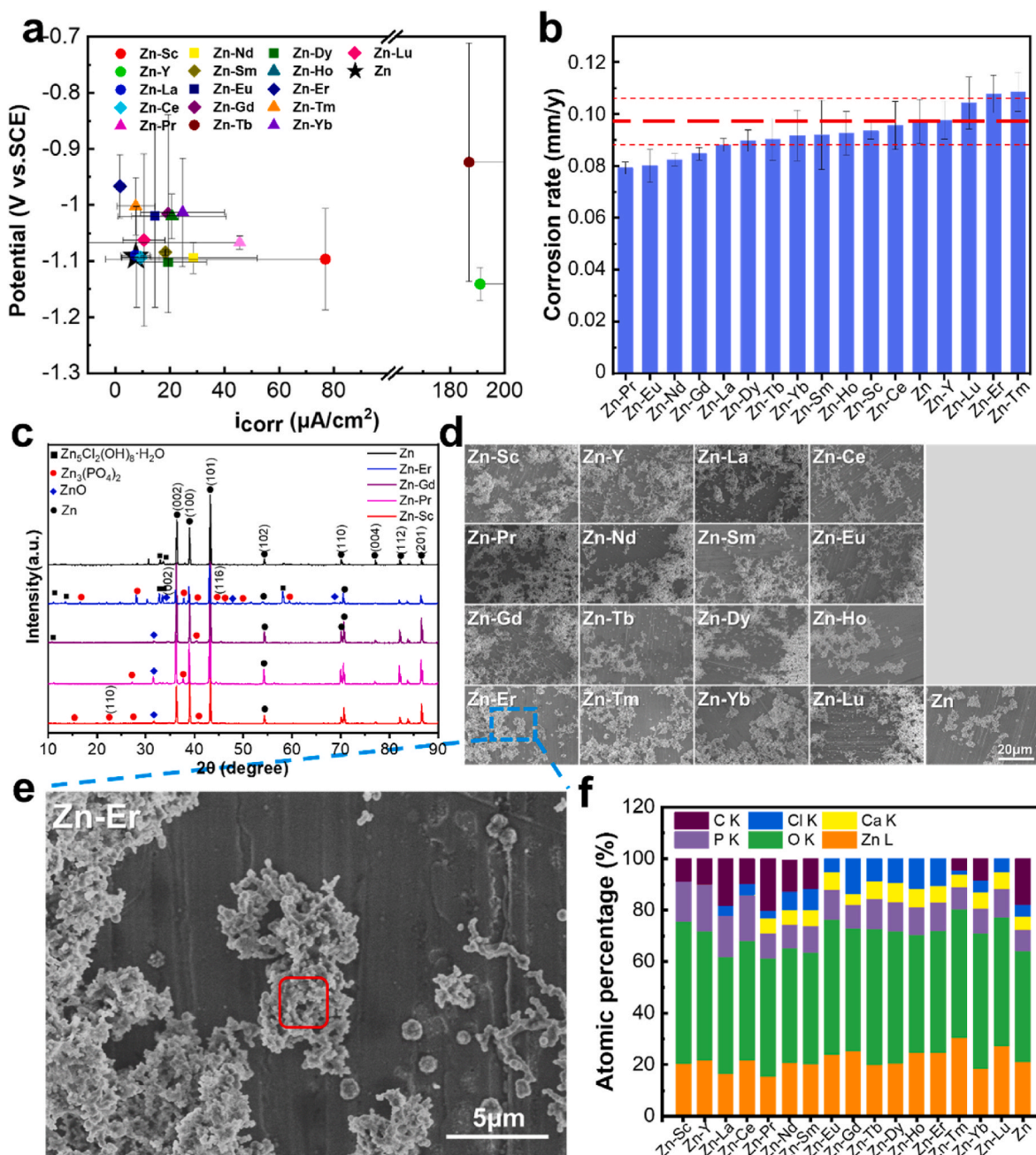


Fig. 3. Degradation properties of the pure Zn and binary Zn–RE alloys: (a) The scatter diagram of corrosion current density and corrosion potential calculated from the electrochemical test. Error bars indicate mean \pm standard deviation ($n = 3$, independent samples). (b) Immersion corrosion rate. Error bars indicate mean \pm standard deviation ($n = 4$, independent samples). (c) XRD patterns of the pure Zn, and the typical binary Zn–RE alloys (Er, Gd, Pr and Sc). (d) SEM micrograph of the corrosion morphology of the Zn and Zn–RE alloys immersed in SBF for 28 days. (e) Magnified corrosion morphology of Zn–Er alloy immersed in SBF for 30 days. (f) Summary of the EDS quantitative analysis on corrosion products on the pure Zn and Zn–RE alloy surface.

superior hardness values at 63.22.

In order to explore the fracture mechanisms of the Zn-RE alloys, the tensile fracture morphology was observed and shown in Fig. S3. The fracture morphologies of Zn-RE alloys suggest roughly three ways of fractures. Pure Zn and Zn-Eu alloy exhibit cleavage fracture with the typical brittle fracture morphology of river pattern (indicated by the red arrows). Cleavage fracture, demonstrating poor ductility, is commonly presented in hexagonal close-packed structure including Zn, which is consistent with the low elongation values in Fig. 2(d). The second fracture model is the quasi-cleavage fracture, i.e., combined brittle and ductile fracture, which are found in five Zn-RE (La, Pr, Nd, Er, and Yb) alloys. The morphology is typically featured with flat “cleavage-like” planes (indicated by yellow arrows), and tearing edges (indicated by blue arrows), and micropores (indicated by green arrow). Most of the Zn-RE alloys (Sc, Y, Ce, Sm, Gd, Tb, Dy, Ho, Tm, and Lu) display more ductile fracture mode with microvoid accumulation fracture.

3.3. In vitro degradation behaviors

3.3.1. Electrochemical tests

The OCP curves and the electrochemical polarization plots of the Zn-RE alloys and pure Zn are shown in Fig. S4 and Fig. S5, respectively. It can be seen that the open circuit potential values of all Zn-RE binary alloys are within the range of $-1.2\text{ V} \sim -0.9\text{ V}$ which is close to that of the pure Zn, -1.18 V . The corrosion parameters including corrosion current density (i_{corr}) and the corrosion potential (E_{corr}) obtained using Tafel extrapolation method and were listed in Table S2.

Fig. 3(a) is the scatter diagram of the corrosion current density and the corrosion potential of the Zn-RE alloys. Pure Zn sits on the bottom-left corner of the scatter diagram with the combined corrosion potential of -1.09 V and corrosion density of $7.8\ \mu\text{A}/\text{cm}^2$. Roughly, there are three groups of the Zn-RE alloys categorized in this diagram. Both Zn-Tb and Zn-Er present higher corrosion potential values, -0.92 V and -0.97 V , respectively. However, the corrosion current density varies largely from $187\ \mu\text{A}/\text{cm}^2$ for Zn-Tb to $1.76\ \mu\text{A}/\text{cm}^2$ for Zn-Er. The second group of Zn-RE alloys gathers at the corrosion potential of $-1.0 \sim -1.02\text{ V}$, including Zn-Tm, Eu, Gd, Ho, and Yb with increased corrosion current density from $1.76\text{--}24.7\ \mu\text{A}/\text{cm}^2$. The rest Zn-RE alloys are distributed at relative low corrosion potentials close to Zn from -1.07 V to -1.1 V with scattered corrosion current densities. Among these, Zn-Lu and Zn-Pr present corrosion current densities of 10.5 and $45.6\ \mu\text{A}/\text{cm}^2$. Zn-RE (La, Ce, Sm, Dy, Nd and Sc) alloys present similar corrosion potential of -1.1 V with increased corrosion current density values. Zn-Y exhibits highest corrosion current density of $190.9\ \mu\text{A}/\text{cm}^2$. Low corrosion potential suggests more difficult to start the corrosion and low corrosion current density demonstrates low electrochemical corrosion rate, therefore, it can be concluded that Zn-Er is relatively more difficult to be corroded in a lower rate while Zn-Y is relatively easy to be corroded in a higher speed.

3.3.2. Immersion test

Fig. 3(b) shows the corrosion rates of the Zn-RE alloys that were immersed in SBF for 28 days via the weight loss method. It can be seen that the variations of the corrosion rates of the Zn-RE alloys mostly fall into the range of $0.0792\text{--}0.1085\text{ mm/y}$ ($79.2\text{--}108.5\ \mu\text{m/y}$) and close to that of the pure Zn. Four Zn-RE alloys (Tm, Er, Lu and Y) possess relatively higher corrosion rates than pure Zn, while there are four Zn-RE alloys including Zn-Pr, Zn-Nd, Zn-Eu and Zn-Gd, that corrode slower than pure Zn. Compared with the calculated corrosion rates based on the electrochemical tests, the corrosion rates obtained from immersion tests are generally lower and the variations among the pure Zn and Zn-RE alloys are not that significant. Both tests exhibit Zn-Y with quite high corrosion rate, however, the corrosion rate ranking for the pure Zn and Zn-RE alloys from the electrochemical test and immersion test is very different. The electrochemical test is a real-time measurement of the corrosion process by applying a small range of voltage onto the alloys.

While the corrosion rate calculated using the weight loss method from the long-term immersion tests reflects the average corrosion rate of the alloys for a specific time duration. So the corrosion rates based on the two tests vary a lot.

The macroscopic surface morphologies of the Zn-RE alloys after 28 days' immersion in SBF are shown in Fig. S6. All the Zn-RE alloys surfaces were covered with a thin layer of white corrosion product, however, the coverage area on each Zn-RE alloy surface is different. The surfaces of Zn-Y, Zn-Er, Zn-Tm and Zn-Lu alloy are fully covered with thick corrosive product layer, corresponding to higher corrosion rates and severe corrosion. More than half surface is covered for the Zn-RE (Sc, Ce, and Ho) alloys, which is similar to pure Zn. The rest of the Zn-RE alloys (La, Pr, Nd, Eu, Gd, Tb, Dy, Sm and Yb) exhibit clearly grinding tracks, metallic shiny surface and less than half covered surface, suggesting lower corrosion rates. The morphology observation agrees well with the corrosion rate variations in Fig. 3(b). The XRD patterns of corrosion products of the pure Zn, and typical Zn-RE alloys (Er, Gd, Pr and Sc) are shown in Fig. 3(c) and the XRD patterns of all Zn-RE alloys is shown in Fig. S7. The four Zn-RE alloys and pure Zn show complex phases of the corrosion products, mainly including ZnO, $\text{Zn}_3(\text{PO}_4)_2$, and $\text{Zn}_5\text{Cl}_2(\text{OH})_8 \cdot \text{H}_2\text{O}$ within the corrosion products and Zn peaks are from Zn alloy matrix. The Zn-Er with higher corrosion rate than that of pure Zn (Fig. 3(b)) presents more obvious peaks of ZnO, $\text{Zn}_3(\text{PO}_4)_2$, and $\text{Zn}_5\text{Cl}_2(\text{OH})_8 \cdot \text{H}_2\text{O}$ and the intensities of those peaks are relatively high compared to the Zn peaks in the same pattern. XRD pattern of the Zn-Sc alloy exhibits obvious $\text{Zn}_3(\text{PO}_4)_2$ peaks. While the Zn-Pr and Zn-Gd alloys with less corrosion products on the surfaces present more prominent Zn peaks and less corrosion product phases, confirming lower corrosion rates. The corrosion product phase identification agrees well with the corrosion rate calculation in Fig. 3(b) and corrosion morphology observation in Fig. S6.

Corresponding to the macroscopic images of the corroded Zn-RE alloys in SBF for 28 days, we also characterized corrosion product compositions and microscopic corrosion morphologies of the Zn-RE alloys and pure Zn using SEM and EDS in Fig. 3(d–f) and Fig. S8.

Fig. 3(d) shows the overview corrosion morphology of each Zn-RE alloy at low magnification and Fig. 3(e) exhibits an SEM micrograph of Zn-Er alloy surface with the details of corrosion product at high magnification. After immersed in the SBF for 28 days, the surfaces of Zn-RE alloys and Zn are covered with scattered, globular and also agglomerated microparticles. There are no obvious differences in the microscopic corrosion morphology for the Zn-RE alloys and pure Zn. Fig. 3(e) shows the microparticles corrosion product on Zn-Er alloy surface. EDS was used to analyze the elements in different areas of the corrosion surface of the alloy. Fig. S8 shows the EDS spectra of the selected areas on each of Zn-RE alloys. The main elements found from the agglomerated corrosion products are Zn, O, P, Ca, Cl and C while the main elements for the clear areas are Zn, P, O and Ca, further confirming the corrosion product phases. There are no observable differences on the elemental compositions among each Zn-RE alloys and Zn. Fig. 3(f) summarizes the elemental composition of the corrosion products on the surface of each Zn-RE alloys. It can be seen that the corrosion products of these alloys are similar, and the mainly elements were Zn, P, Ca, C, O and Cl. The proportion of O was the highest, followed by Zn and P.

3.4. In vitro biocompatibility evaluations

3.4.1. Cytocompatibility

Fig. 4 shows the cytocompatibility and hemocompatibility assessments on the Zn-RE alloys and pure Zn. Fig. 4(a) displays the Zn^{2+} concentrations in the extracts of each alloy cultured in the cell media for 24 h. The concentration of RE^{3+} was not able to be detected using ICP-OES due to the low concentrations. The Zn^{2+} concentration released from the Zn-RE alloys and Zn in the cell culture mediums are relatively close within the range of $4.35\text{--}5.29\text{ mg/L}$ and these concentrations are all lower than that of the pure Zn (5.28 mg/L) except Zn-Ho alloy.

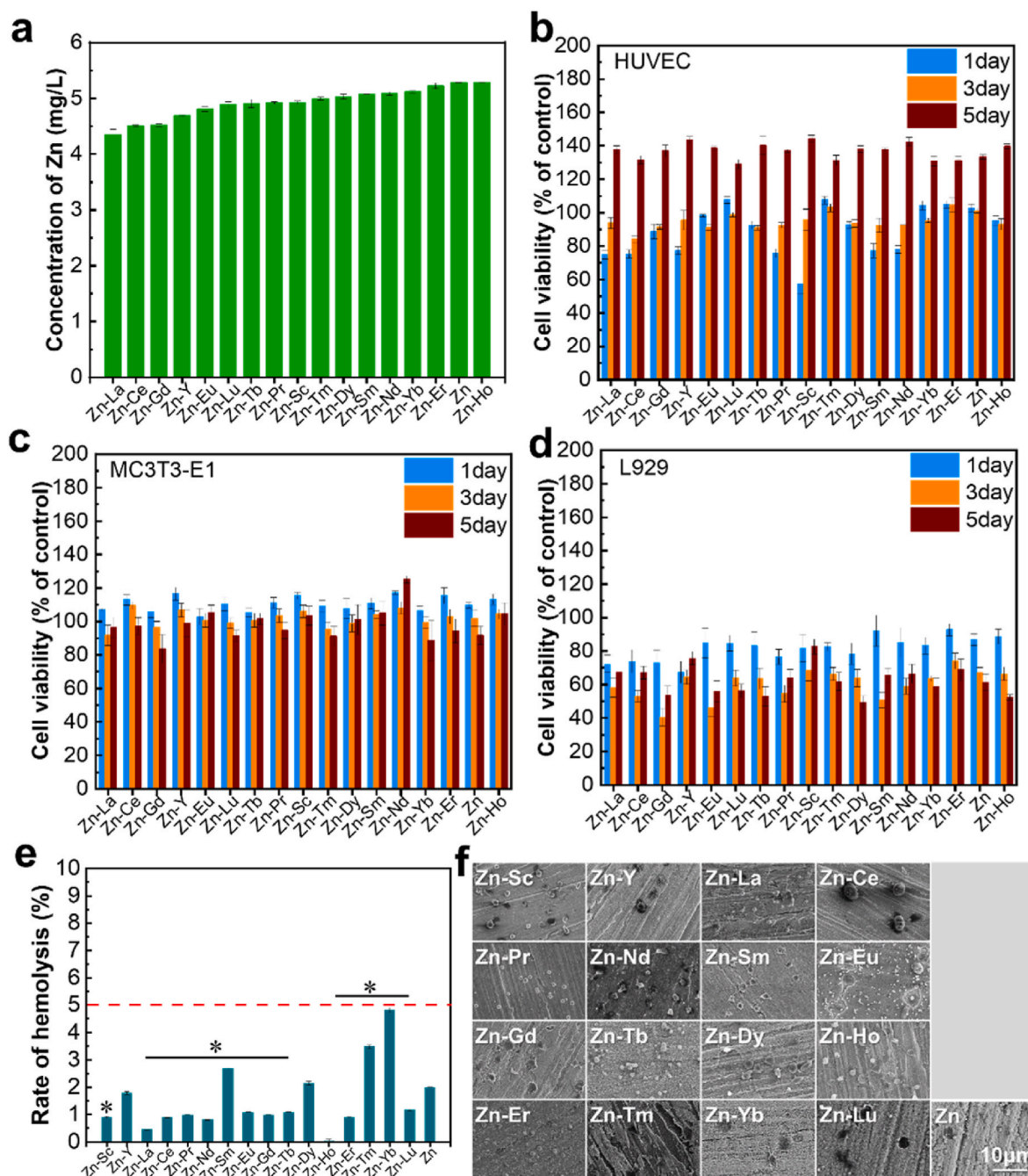


Fig. 4. *In vitro* biocompatibility evaluation of the pure Zn and binary Zn-RE alloys. (a) The concentrations of Zn²⁺ in the extract of cell culture medium. (b–d) Cell viability of HUVEC, MC3T3-E1 cells and L929 cells after cultured with the extract, (n = 5, independent samples). (e) Rate of hemolysis. (n = 3, independent samples), and (f) SEM morphology of platelet adhesion on the surface of the materials. Error bars indicate mean ± standard deviation.

Roughly, the Zn-RE alloys can be divided into four groups in terms of the released Zn²⁺ concentration from low to high, Zn-RE (La, Ce, Gd and Y), Zn-RE (Eu, Lu, Sc, Pr, and Tb), Zn-RE (Tm, Dy, Sm, Nd, and Yb) and Zn-RE (Er and Ho). The variations of the Zn²⁺ concentrations have direct effect on the cytocompatibility.

Osteogenesis and angiogenesis play pivotal roles in skeletal development, and bone fracture healing. The cytocompatibility of the Zn-RE alloys and pure Zn were evaluated using three cell lines, HUVEC, MC3T3-E1 cells and L929 and the cell viability of these cells after co-cultured with the extracts for 1 day, 3 days and 5 days is shown in Fig. 4(b–d), respectively. The HUVEC and MC3T3-E1 cells were cultured in 2-fold diluted extracts of the Zn-alloys and pure Zn (50% of the measured Zn²⁺ concentrations in Fig. 4(a)), while the L929 cells were

cultured in 4-fold diluted extracts of the Zn-alloys and pure Zn (25% of the Zn²⁺ concentrations). Among the viability of three cell lines, HUVEC cells present increased viability with culture time and display the highest overall viability, up to 140% in the 5th day. MC3T3-E1 cells show the overall viability up to 120%, while L929 cells show the lowest viability, lower than 100%.

Fig. 4(b) clearly shows that, other than Zn-Sc alloy in the 1st day with 57.2% cell viability, all other Zn-RE alloys and Zn are all highly cytocompatible to HUVEC because of more than 70% cell viability and also the proliferation promoting effect because of more than 129% cell viabilities in 5th day. After 1-day culture, the Zn-RE alloys (Lu, Tm, Er, Yb, and Eu) exhibit the higher viability from 98.4% to 107.6%. The cell viability from the extract of pure Zn, 102.8%, is also within this range.

Four Zn-RE alloys exhibit relatively lower but very similar cell viabilities around 92.3% including Zn–Gd, Zn–Tb, Zn–Dy and Zn–Ho. The third group of Zn-RE alloys exhibit further lower viability around 76.5% including Nd, Y, Sm, Pr, Ce, and La. It can be seen that the cell viability does not vary along the trend of the Zn^{2+} concentration in the extracts of the Zn-RE alloys and pure Zn, demonstrating the cell toxic effect from the trace amount of the RE^{3+} in the extracts. After 3 days' culture, the cell viabilities of the HUVEC from the extracts of the Zn-RE alloys and Zn vary to different extents. The viability of the first Zn-RE alloys group (Eu, and Er–Lu) decreases slightly to 98% and the viability of the second group (Gd–Ho) remains at 92.3%, while viability of the third group of Zn-RE alloys and Zn–Sc increases great to 93% in the 3rd day. After 5 days' culture, the cell viability of HEUVC from all the materials extracts increased significantly to above $129.1\% \pm 2.7\%$, demonstrating generally lower cytotoxicity than pure Zn and also the excellent cytocompatibility of the Zn-RE alloys to HEUVC with the Zn^{2+} concentrations of 2.175–2.65 mg/L.

Fig. 4(c) shows the cell viabilities of MC3T3-E1 vary within the range of $125.1\% \pm 5.4\%$ – $84\% \pm 1.7\%$ after co-cultured with the 50% concentrated extracts of the Zn-RE alloys and pure Zn for different time durations, suggesting the excellent cytocompatibility of the Zn-RE alloys to MC3T3-E1. Different from the HUVEC, the viabilities of MC3T3-E1 cells with the materials extracts decrease roughly by 5%–10% ($109.7\% \pm 1.7\%$ – $96.5\% \pm 3.7\%$) with the cell culture time from 1 day to 3 days. The viabilities further decrease ~10% for most of the Zn-RE alloys from 3 days to 5 days' culture, however, Zn-RE (La, Eu and Nd) show increased viability in the 5th day, especially Zn–Nd with the viability of $125.1\% \pm 2.1\%$. There is no much change in cell viability from 3 to 5 days for alloys of Zn-RE (Sm, Tb, Dy and Ho). It also can be seen that the variation of the viability of MC3T3-E1 does not follow the tendency of the Zn^{2+} concentration.

Fig. 4(d) shows the cell viabilities of L929 cell after co-cultured with 4-fold diluted Zn-RE alloys and pure Zn extracts for 1, 3 and 5 days. It is generally lower than the HUVEC and MC3T3-E1 within the range of $86.9\% \pm 3.5\%$ – $61.5\% \pm 4.9\%$ from 1 to 5 days. After 1 day culture, all the viability of the L929 cells with alloys' and pure Zn extracts are higher than 70%, suggesting acceptable cytocompatibility toward L929 cells with Zn^{2+} concentration at 1.3 mg/L. The cell viability decreases for all the Zn-RE alloys and pure Zn after 3 days co-culture to lower than 70%. However, in 5th day, the cell viability increases to varied extent for the Zn-RE alloys (Sc–Gd) and it also further decreases for the Zn-RE alloys (Yb–Lu) and pure Zn. The cell viability of the L929 cells does not vary along the fluctuation of the Zn^{2+} concentrations, indicating that the cell viability is the synchronized effects of both Zn^{2+} and RE^{3+} . It can be seen that the viabilities of L929 cells co-cultured with the Zn-RE alloys improve along with time compared to pure Zn from 1 day to 5 days.

The cell morphologies of the three types of cells after co-cultured with the diluted extracts of the Zn-RE alloys for 5 days are shown in Fig. S9. The cell morphology variations among the Zn-RE alloys and pure Zn are consistent with the viability variations in Fig. 4. For HUVEC cells, the cell density on each Zn-RE alloy and pure Zn surfaces are high with whole field of vision covering and close cell contact. It also can see that there is a large number of apoptotic cells in round shape on the 5th day, which may be related to cell adhesion inhibition. MC3T3-E1 cells cultured in the extracts of the Zn-RE alloys and pure Zn are in the elongated or star shapes with some round dead cells. The inhibitory effect of the extracts on L929 cells is strong, so the activity of L929 cells is low after 5 days of culture by showing a large number of round dead cells in the field of vision.

3.4.2. Hemocompatibility

Fig. 4(e) is the hemolysis rate of New Zealand rabbits blood cells after co-cultured with the extracts of the Zn-RE alloys and pure Zn. The hemolysis rate of all materials is less than 5% and all alloys and pure Zn can be categorized into blood compatible materials according to the requirements of ISO 10993-4 standard. The hemolysis rates of Zn–Ho

and Zn–La present extremely low values at 0% and 0.45%, respectively. Most of Zn-RE (Sc, Ce, Pr, Nd, Gd, and Er) alloys exhibit also very low rate range from 0.8% to 0.98%. While the hemolysis rates of the Zn-RE (Tb, Eu, Lu and Y) alloys are in relative higher range of 1.1%–1.8%. Although the rest four Zn-RE alloys exhibit higher hemolysis rates (2.1%–4.8%) than that of the pure Zn ($1.96\% \pm 0.04\%$), those values are still below 5%. Fig. 4(f) shows the blood platelet adhesion morphology on the surface of the Zn-RE alloys. There are no obvious platelet aggregations can be observed from any Zn-RE alloys or pure Zn, suggesting that the platelets on these Zn-RE alloy samples were not activated. The morphological changes of platelets can be divided into five stages [46]: round, dendritic, spread-dendritic, spreading and fully spread, which correspond to the activation level from never activated to fully activated. The platelets on the surface of the Zn-RE alloys are evenly distributed and discrete. The platelets on the surface of Zn-RE alloys (Sc, Ce, Pr, Er, and Ho) are spherical, while the platelets on the surfaces of other Zn-RE alloys, especially the Zn–Sm, Zn–Dy, and Zn–Yb, present pseudopods, or spread dendrites, which agrees with the hemolysis results.

3.5. In vivo tissue biocompatibility

Zn–La, Zn–Ce and Zn–Nd alloys were selected as example alloys for *in vivo* biocompatibility evaluations. Fig. 5 shows the bone-implant interface of the cranial view of the implanted Zn-RE alloys in tibia for 6 and 12 weeks with the corresponding element mapping images. From the overview SEM images in Fig. 5(a), we can see that after 6 weeks of implantation, the three alloys all have combined with the bone tissues, although there are still some visible dark strip gaps along the interfaces. The high magnification images on the gap areas were shown as the insets and the detailed composition analysis with elemental mapping are also shown on the right-hand side panel. The elemental mapping of C well overlaps with the dark strip area without any other elements, suggesting that the embedding resin filling up the gap between the implants and the bone tissues. Therefore, the dark strip areas mapped with C demonstrate the non-bonding areas. We can see that the carbon mapped areas are shown in the interfaces between pure Zn implant and also the Zn-RE alloys implants with the bone tissues and the C mapping intensity in pure Zn seems higher than the Zn-RE alloys. Zn is mainly distributed in the implant region with a clear boundary along the implant interface for pure Zn, Zn–La and Zn–Ce alloys. For the Zn–Nd alloy, the Zn element distributes not only along the interface but also extends to the gap area, which demonstrates the better tissue-implant binding capability. Although the alloy concentration of REEs and the intensity of REEs mapping are low, we still can find the REEs mapping overlaps with the distribution area of Zn. The elemental mapping of P, O, and Ca appearing in the surrounding bone tissue areas can be attributed to hydroxyapatite as the main composition of the bone tissues. After 12 weeks' implantation, Fig. 5(b) shows the similar interface morphology and also the compositions of the implants and the tibia tissues. There are more Zn mapped out in the gap areas between the implants and the bone tissues for Zn–La and Zn–Ce alloys, demonstrating that the Zn-RE alloys exhibit better osseointegration capability with the implantation time.

Fig. 6 (a) shows the hard tissue sections of the bone-implant interfaces after 6 weeks and 12 weeks' implantation at low and high magnifications. The combination of the implant with bone tissue can be seen more clearly. The gaps between the implants and the bone tissues seem not as obvious in the Zn–La, Zn–Ce and Zn–Nd alloys as that in the pure Zn. Overall, the osseointegration of the implanted Zn-RE (La, Ce and Nd) alloys were better than that of the pure Zn control group. In the pure Zn group, there are still a small number of weak binding areas, which are separated by a layer of fibrous connective tissue. It suggests that the addition of REEs may have positive effect on osseointegration. The specific mechanism needs further study. In order to evaluate the potential risks of implants *in vivo*, the effects of implants degradation on biological tissues were explored, and the *in vivo* biocompatibility was

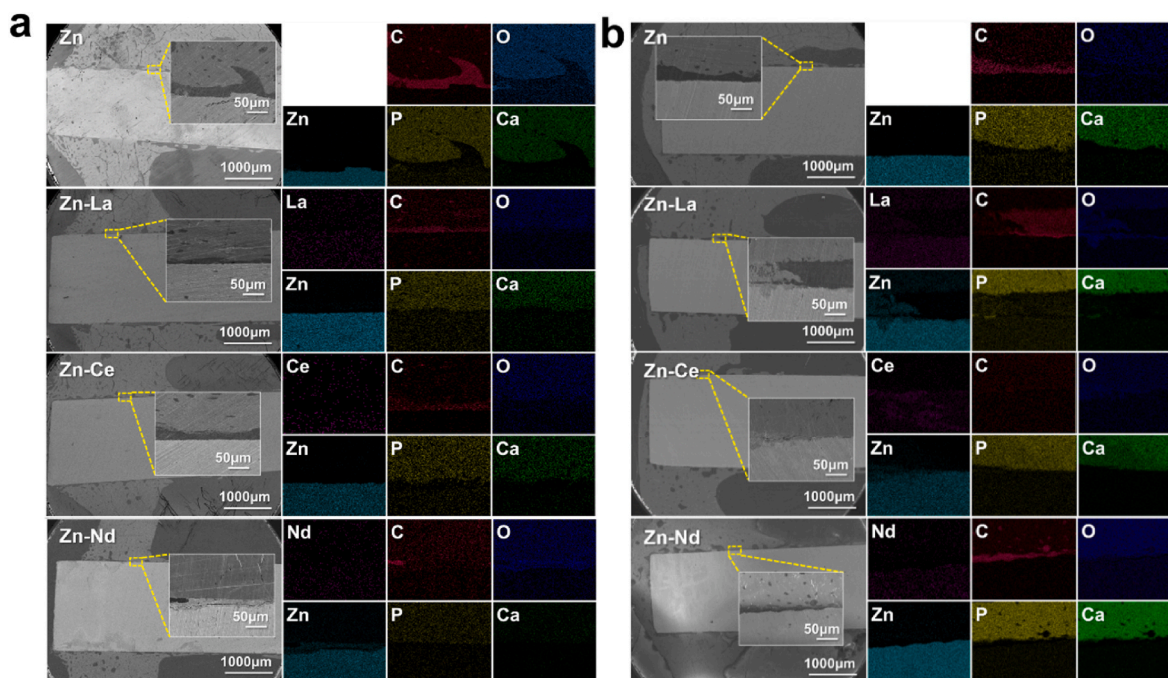


Fig. 5. The transverse section of the implanted Zn-RE alloys in tibia: the cross-section morphology and the EDS elemental mapping of the bone-implant interface for the pure Zn and Zn-La, Zn-Ce and Zn-Nd alloys. (a) 6 weeks after implantation. (b) 12 weeks after implantation.

characterized. Fig. 6 (b) displayed the histological examination results of the organs including heart, liver, spleen, lungs, and kidneys in each group. No obvious abnormalities were observed in the organs, such as appearance color difference or tissue ulceration, and no obvious inflammatory reaction or bone necrosis was observed around the bone tissues of the implants by naked eye. There were no pathological changes in all groups.

After 6 weeks of implantation, there was no observable gap between all implants of the pure Zn and Zn-RE alloys and the bone tissues, while there were some gaps appearing for the implants of the pure Zn, Zn-La, and Zn-Ce with the bone tissues after 12 weeks implantation *in vivo*. The binding between the Zn-Nd implant and the bone tissue was still quite tight with less gap area. It suggested the start of the degradation of pure Zn, Zn-La and Zn-Ce, and the degradation would occur for Zn-Nd for long implantation time. This observation agrees well with the *in vitro* degradation results in Fig. 3(b) as Zn-Nd exhibited lower degradation rate than that of the pure Zn, Zn-La and Zn-Ce. This phenomenon is consistent with our expectations for the materials to gradually degrade after 3 months' implantation as mechanical supporting scaffold.

Fig. 6 (c) is a histogram of Zn^{2+} concentration in rabbit serum, which is about 1.25 μg/mL. There was no significant difference among the concentration of Zn ions at 6 weeks and 12 weeks, indicating that Zn^{2+} in blood could be metabolized normally and did not accumulate. REEs could not be detected from rabbit serum. This demonstrated that the Zn-La, Zn-Ce and Zn-Nd alloys were biocompatible with blood, tissue and organs.

4. Discussions

4.1. Effect of REEs on the properties of Zn alloys

In this study, we systematically investigated the microstructure, mechanical properties, bio-corrosion behaviors, *in vitro* cell and blood biocompatibility and *in vivo* tissue biocompatibility of the 16 Zn-0.2 wt% RE binary alloys. After the thorough comparisons with the pure Zn, we summarized the main properties of Zn-RE alloys into Fig. 7. It is evident that significant improvement was achieved in mechanical properties.

Further comparisons demonstrated that the 16 Zn-RE alloys can be categorized into groups with similar properties. The variations in all these properties among the Zn-RE alloys also exhibit a certain trend. The Y, Ho, and Lu alloyed into Zn greatly enhanced most of the properties. On the other hand, the Zn-Eu, Zn-Gd, and Zn-Dy alloys present relatively low values of most of the properties. These findings are helpful in selection of appropriate alloys for different applications.

The addition of REEs to Zn has a significant strengthening effect on the mechanical properties compared to the pure Zn. The mechanism can be attributed to second phase reinforcement [47]. Due to the low solubility of REEs in Zn, the alloying elements are mainly present in the form of the second phase ($ReZn_{11/12/13}$). When the second phase is uniformly distributed in the matrix phase in the form of fine diffuse phase, it would play the role of reinforcement to significantly enhance strength of the alloys. Thus, all the Zn-RE alloys are strengthened in the aspects of TYS, UTS and uniform elongation rates compared to those of the pure Zn. The second phase in the Zn matrix results in a large number of dislocations during deformation, which improves the strain-hardening rate and improves the threshold of the material plastic instability criterion. According to the Considère criterion for plastic instability [48], the uniform elongation of the material is improved. Moreover, we found that the distributions of second phases on the matrix of the Zn-RE alloys vary a lot, which could be a key factor for the different strengthening effects from different REEs. As evident in Fig. 1(b), the second phase appears in Zn-Y and Zn-Ho alloys with higher volume proportion, more uniform distribution and larger size, especially in Zn-Y. Thus, the strength of both Zn-Y and Zn-Ho are significantly higher or close to 200 MPa comparing to Zn (3–3.5 times higher), which can be used as clinical devices such as bone screws [47]. With similar volume proportion of the second phase but less uniform distribution, Zn-Ce, Zn-Yb and Zn-Lu exhibit relatively high strengths up to 155 MPa (Figs. 7 and 2(a & b)). When the second phases present in the matrix with either low volume, or high volume but not uniform, the strengths of Zn-RE alloys can be enhanced to a less extent (2.3–2 times higher). Correspondingly, the UEs of the Zn-RE alloys was improved with the addition of REEs compared to pure Zn. While the improvement tendency of UE is roughly opposite to that to UTS, Lu and Ho presents the capability of highly improving both

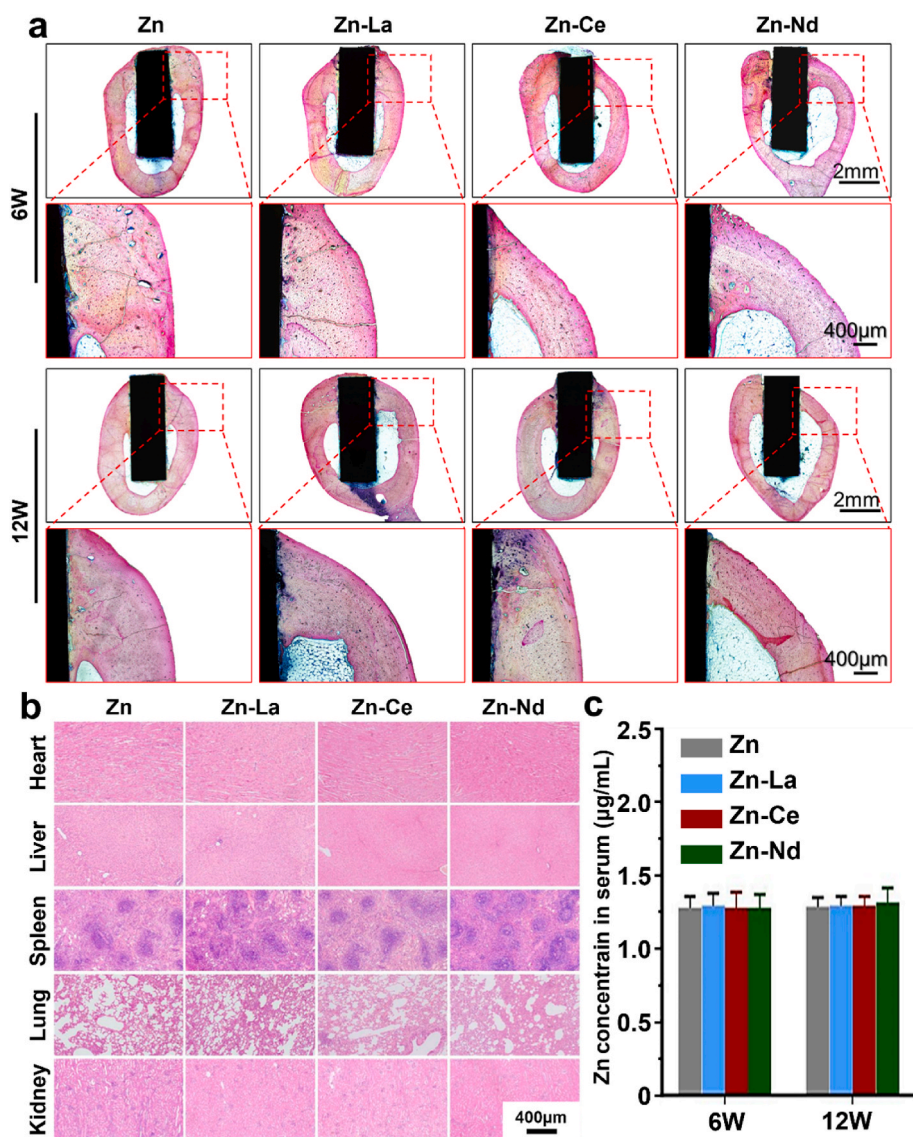


Fig. 6. (a) The transverse section of the implanted Zn-RE alloys in tibia: hard tissue sections of the bone-implant interfaces after 6 weeks and 12 weeks implantation periods. The red rectangles are zoomed in for clarity. (b) HE staining of rabbit heart, liver, spleen, lungs, and kidney after 12 weeks. (c) The Zn^{2+} concentration in the rabbit serum.

strength and ductility and Eu is relatively at the low end of both. Consistent to the UTS, it is still Y, Ho, and Lu that increases the CYS to higher extent and the Gd, Eu and Dy are in the low end with decreased CYS (Fig. 7).

Table S3 summarized the properties of other Zn alloys and compared to the properties of the Zn-0.2 at%RE alloys. It can be seen that the Zn-RE binary alloys aligns well with other binary Zn alloys in terms of mechanical properties. The as-extruded Zn-RE alloys are similarly strong with the commercial Zn alloys (ZnMgAlCu) with the UTS at 188–219 MPa, and CYS at 211 MPa compared to 185–228 MPa and 165–230 MPa while the elongation is much lower than that of the commercial ZnMgAlCu [49]. Although the strength of Zn-RE alloys is not higher than that of Zn-Mg, Zn-Cu, and Zn-Ag alloys, considering that the addition amount of REEs in Zn is from 0.14 wt%–0.53 wt%, the strengthening effect is still relatively efficient proportion to the alloying amount comparing to 2–4 wt%Cu [50], 0.8–1.6 wt%Mg [51] or 2.5–7 wt%Ag [52]. Compared to the similar alloy amount and extrusion processing, Zn-RE alloys exhibit higher UTS than Zn-Sr alloys and greater strengthening effect as well [21]. Ternary Zn alloys with Mg, Cu and/or Li possess even higher mechanical properties, suggesting that it is

possible to further improve mechanical properties of Zn-RE alloys with third elements.

As shown in Figs. 3 (b) and Fig. 7, the degradation rates of the Zn-RE alloys are closely in the range of 110 μm/y ~80 μm/y. Compared to pure Zn, the degradation rates of the Zn-RE (Tm, Er, Lu and Y) alloys are higher while the addition of other REEs slows down the degradation process. Based on the electrochemical potential of four REEs (listed in Table S4), Tm, Er, Lu and Y, there is no specific reason or trend for these four REEs over other REEs to increase the corrosion rate of Zn. The electrochemical measurements on the Zn and Zn-RE alloys also exhibit both increased and decreased corrosion rates with different REEs in SBF and the trend is difficult to conclude. All the REEs possess higher electrochemical potential from -1.991 V to -2.379 V than that of Zn at -0.76 V, suggesting the REEs alloyed in Zn could slow down the degradation rate because Zn-RE alloys are relatively easy to react with environments to degrade and the resulted oxides layers could passivate and prevent further corrosion process [53]. However, it is commonly found the corrosion rates of Zn alloys, Zn-x(Mg, Ca, Sr, Li, Mn, Fe, Cu or Ag, 0.1–0.8 wt%) [27], were all enhanced regardless of the electrochemical potential differences. The reason was attributed to the


Zn-0.2at%RE Alloys		High 				Low
Mechanical properties	UTS	Y, Ho (219–188MPa)	Ce, Yb, Lu (155–152MPa)	Nd, Er, Sc, Sm, Pr (146–134MPa)	La, Eu, Dy, Gd, Tm, Tb, Zn (122–104MPa, 63MPa)	
	UE	La, Tb (14.4%, 13.2%)	Sm, Er, Lu, Gd, Ho (12.9%–12.0%)	Dy, Ce, Pr, Tm, Nd (11.9%–10.5%)	Sc, Yb, Y, Eu, Zn (8.8%–6.3%, 4.5%)	
	CYS	Y (211MPa)	Ho, La, Lu (137–126MPa)	Ce, Sc, Nd, Yb (121–99MPa)	Sm, Zn, Gd, Pr, Eu, Dy, Tb, Er, Tm (90–69MPa)	
Static degradation	Corrosion rate	Tm, Er, Lu, Y (108–98 $\mu\text{m}/\text{y}$)	Zn, Ce, Sc, Ho (97.2–92.7 $\mu\text{m}/\text{y}$)	Sm, Yb, Tb, Dy, La (92.0–88.1 $\mu\text{m}/\text{y}$)	Gd, Nd, Eu, Pr (84–79 $\mu\text{m}/\text{y}$)	
Cytocompatibility: Cell viability in 5 days	HUVEC	Sc, Y, Nd, Tb (144%–140%)	Ho, Eu (139%–138%)	Dy, Sm, La, Gd (138%–137%)	Zn, Ce, Tm, Er, Yb, Lu (133%–129%)	
	MC3T3-E1	Nd, Eu, Sm, Ho, Sc (125%–103%)	Tb, Dy, Y (101%–99%)	Ce, La, Pr, Er (97%–92%)	Zn, Lu, Tm, Yb, Gd (91%–84%)	
	L929	Sc, Y (83%, 76%)	Er, La, Ce, Nd, Sm, Pr (68%–64%)	Tm, Zn, Yb, Lu, Eu (62%–55%)	Gd, Tb, Ho, Dy (53%–49%)	
Hemocompatibility	Hemolysis	Ho, La (0%–0.5%)	Nd, Er, Ce, Sc, Gd, Pr (0%–1.0%)	Tb, Eu, Lu, Y (1.1%–1.8%)	Zn, Dy, Sm, Tm, Yb (2.1%–4.8%)	

Fig. 7. Properties comparison among the pure Zn and Zn-RE alloys.

preferential corrosion in the formed intermetallic phases. Although our corrosion results are scattered within the 16 REEs, the spanned range of corrosion rates (110–80 $\mu\text{m}/\text{y}$) is comparable with most of the Zn alloys, Zn-xAg (79–84 $\mu\text{m}/\text{y}$) [52], Zn-xCu (60–160 $\mu\text{m}/\text{y}$) [54], Zn-1Mg/Ca-1Ca/Sr (90–110 $\mu\text{m}/\text{y}$) [55], Zn-1.5Mg-0.1(Ca, Sr) (105–110 $\mu\text{m}/\text{y}$) [56] and Zn-xMg-0.1Mn (85–115 $\mu\text{m}/\text{y}$) [29], in a variety of simulated body solutions. The corrosion rates at 85–120 $\mu\text{m}/\text{y}$ corresponds to the value 16.5–23.0 $\mu\text{g}/\text{cm}^2/\text{day}$ [51], which is negligible compared with the Recommended Dietary allowance (RDA) and Recommended Upper Limit for Zn at 15–40 mg/day [57]. Therefore, the Zn-RE alloys would be one of the accepted biodegradable materials for biomedical implants and devices.

Biocompatibility assessment using cell model is an essential method for metallic materials. Our assessment results for the Zn-RE alloys comparing to pure Zn are shown in Fig. 7. The Zn-RE alloys show better cytocompatibility with the HUVECs than MC3T3-E1 and show highest sensitivity to the L929 cells, which is consistent with other Zn alloys cytocompatibility assessments [27]. Furthermore, it also can be found that the general cytocompatibilities of the Zn-RE alloys are improved with the culture time expanded from 1 day to 5 days as the Zn moves from the at relatively high position to low value side, suggesting more Zn-RE alloys exhibit overall improved cytocompatibility probably owing to the addition of REEs. By comparing the cell viabilities among Zn-RE alloys, we can find that the Lu, Ho, and Y, especially Ho, are the three typical REEs showing superior excellence in cytocompatibility with all three cell lines. On the other hand, Dy, Gd and Eu appear in the lower end more frequently. The research on the cytotoxicity testing of the Zn alloys always depend on the cell lines, and the experimental setup. Despite this, our observations are in a good agreement with other cytocompatibility studies on Zn alloys for biomedical implants and devices purpose. Hermawan et al. [19] studied thoroughly on the cytotoxicity evaluation of Zn-3Mg compared to Zn from three cell-materials interaction parameters: cell health, functionality and inflammatory response. The Zn^{2+} concentration is 0.5 mg/L from the alloy extract and the viability of the Normal Human Osteoblast (NHOst) primary cells was reduced by ~50% through an induction of apoptosis at day 1, however, cells were able to recover at day 3 and 7. Cytoskeletal changes were observed but without any significant DNA damage and without significant mineralization process variations. It is also found that the cells underwent a healing process after exposure to the alloys, probably from the alloying element of Mg. Different phenomenon was found from Zn-Li alloys [58], the addition of Li from 0.2 wt% to 1.4 wt%

deteriorated the viability of L929 cells at all concentrations compared to pure Zn. Therefore, in summary, the Zn-RE alloys present outstanding cytocompatibility to three cell lines with much higher Zn^{2+} concentration in the extracts (4.35–5.29 mg/L). Further study with quantified REEs concentration in the extract will be carried out for more detailed factors of cell and materials interactions.

It has been reported that the ions of certain REEs could stimulate the seed cell proliferation and osteogenic differentiation and activate osteogenic signaling pathways [6], and further to promote new bone formation. For example, La^{3+} exhibited a bidirectional concentration dependence on bone marrow stromal cells (BMSCs) differentiation [39–41], while Ce^{3+} can promote collagen deposition, osteoblast formation and bone regeneration [42]. Similarly, Nd^{3+} in the safe concentration range showed inhibitory effect on osteoclasts [43]. Therefore, we chose three Zn-RE alloys (La, Ce and Nd) to assess the *in vivo* degradation, biocompatibility and bone implantation possibility with pure Zn as control. All implants maintained their integrity within 12 weeks. All the implants demonstrated good biocompatibility with no signs of osteolysis, deformity or dislocations. The microscale observation on the bone-implant interface using SEM and EDS demonstrates better osteogenesis and osteointegration from the three Zn-RE alloys than that of pure Zn. Similar to other Zn alloys [27], including Zn-0.1Sr, Zn-0.8Ca and Zn-0.8 Mg, the addition of the REEs is able to promote the bone tissue and materials interactions [22], such as osteoconductivity, angiogenesis, osteogenecity and osteoinductivity, while the *in vivo* biocompatibility is satisfied without raising any concerns in 6 weeks–24 weeks implantation time [59]. Zn-2Mg was specifically investigated and the results showed comparable mechanical properties with the commercially used Mg-4Y-3RE but nine times lower degradation to ensure sufficient mechanical integrity and low doses of released ions [60]. However, the low ductility (~5%) and high Young's modulus (~90 GPa) was pointed out as the disadvantage of the Zn-2Mg. Zn-0.08 wt%Mg was the first formulated biodegradable metal that satisfied benchmark values desirable for endovascular stenting [61]. One issue with Zn-0.08 wt%Mg was the signs of age hardening and strain rate sensitivity, which should be addresses before using this for stent implants. The further work on *in vivo* investigation of Zn-RE alloys could be focused to tackle these questions.

4.2. REEs alloying effects on biodegradable metals

REEs have been recognized as an important strategic resource to

optimize materials' physical, chemical and mechanical properties as dopants or alloying elements due to their unique electronic arrangement characteristic, large ionic radius and strong metallic activity [62]. In the last decade, REEs gradually participate in the development of functional materials for bone regeneration [63]. Other than the FDA approved Mg-RE alloys (WE43, Mg-4Y-3RE-0.4Zr) for orthopaedic surgery [64], single REEs were specifically alloyed into biodegradable Mg metals to improve the mechanical properties, corrosion resistance and also purity of Mg melts [1]. The studies on the binary Mg-RE alloys like Mg-Sc [65], Mg-Dy [66], Mg-Gd [7], Mg-Ce/Nd/Dy [67], the tertiary Mg-Ag-Y alloy [68], and Mg-Zr-Sr-Sc [69], Mg-Zr-Sr-Ho [70], Mg-Nd-Zn-Zr [71] and Mg-Al-Zn-Y alloy [72] are very selective and scattered. Our colleagues have conducted a systematic investigation on all 16 Mg-RE alloys with properly varied alloying concentrations [38]. As much as we are aware, the effect of REEs in the biodegradable Zn was comprehensively studied for the first time in this work. To fully understand the role of REEs in biodegradable metals [53], we compared the Zn-RE alloys system and Mg-RE alloys system from the design principles of biodegradable metallic alloys for biomedical implants [73] from the following aspects, alloying concentration, microstructure, mechanical properties, degradation properties, and *in vivo* and *in vitro* biocompatibility. The comparison results are summarized in Fig. 8.

4.2.1. Alloying concentrations and microstructures

The composition selection of the experimental binary Zn-RE and Mg-RE alloys mainly depends on the maximum solubilities of REEs in Zn and Mg, respectively. For Zn, the solubilities of all 16 REEs are all very low, hence, we chose on single atomic concentration for all REEs at very low values, 0.2 at%, while the corresponding weight concentrations vary from 0.14 wt% for Sc to 0.53 wt% for Lu depending on the atomic weight of each REE. The detailed compositions for the Zn-RE alloys were characterized using ICP-OES and shown in Table S1. On the other hand, the 16 REEs show three maximum solubility ranges in Mg [38], <20 wt%, 20–25 wt% and >25 wt%. Correspondingly, 1 wt% and 3 wt% were selected for Sc, Y, La, Ce, Pr, Nd, Sm, Eu and Yb; 1 wt% and 5 wt% Gd and Tb were alloyed into Mg; while 1 wt% and 10 wt% were adopted for Dy, Ho, Er, Tm and Lu. All the Zn-RE and Mg-RE alloys were formed from hot extrusion. With alloying of the REEs, the microstructures of

both Zn-RE and Mg-RE alloys were refined with the grain sizes of the alloys are reduced compared to the pure Zn and pure Mg, respectively, although the grain sizes of the alloys vary widely from different types of REEs and from different concentrations of REEs. Furthermore, second phases were found from both alloys as well in spherical or ribbon shapes from optical microscopy observation and confirmed by XRD. Second phase precipitation of REEs in Mg-RE alloys is preferentially $RE Mg_{12}$ phase [38], whereas three secondary phases, $RE Zn_{13}$, $RE Zn_{12}$ and $RE Zn_{11}$ precipitate preferentially in Zn-RE alloys. The refinement effect of REEs to Zn or Mg could be attributed to the formation of diffusely finer REE-rich second phase ($RE_x Zn/Mg_y$ phase) that can act as a heterogeneous nucleation of α -Zn phase [74]. As revealed in Fig. 1(b), Zn-Ho, Zn-Y, and Zn-Lu in this study, which have the finely dispersed second phase, enhanced mechanical strength was reflected from the microstructures.

4.2.2. Mechanical properties

Due to the high values of TYS, UTS and elongation of pure Mg, these values of the Mg-RE alloys are generally higher than those of Zn-RE alloys. However, by comparing the enhancing factor of the REEs to the Zn and Mg, it can be found that the addition of 0.27 wt%Y to Zn can increase the UTS up to 3.5 times from 63 MPa to 219 MPa, while the addition of 1 wt%Ce to Mg increased the UTS up to 1.7 times. Furthermore, the highest improvement of elongation of Zn by adding 0.5 wt%Ho is 3.2 times, which is similar to that of Mg by adding 1 wt% Sm. When further comparing the summary of the mechanical properties of Zn-RE alloys (Fig. 2(g) vs. Fig 14 in Ref. [38]), the mechanical properties of Zn-RE alloys are all in the first quadrant, suggesting all the Zn-RE alloys possess higher strength and ductility than pure Zn. In contrast, there were in total 10 Mg-RE alloys with 8 REEs, out of 33 Mg-RE alloys, presenting in the first quadrant, suggesting that most of the Mg-RE alloys show reduced mechanical properties compared to pure Mg. Thus, the enhancement efficiency of REEs to pure Zn is higher than those to enhance pure Mg, especially considering of the very low addition amount of REEs in Zn. The purely improving effect of REEs on the Zn mechanical properties still need more comprehensive study with different concentrations of REEs and deeper investigation on strengthening mechanism.

Properties	Mg-RE alloy ⁴⁵			Zn-RE alloy (this work)		
Solubility & 2nd phase	Three solubility ranges (wt%): <20%, 20–25% & >25%; $RE Mg_{12}$			The solubility range (wt%): 0.14–0.53%; $RE Zn_{13}$, $RE Zn_{12}$ and $RE Zn_{11}$		
Mechanical properties	The maximum UTS was achieved from Mg-1 wt%Ce at 358 MPa comparing to the pure Mg at 210 MPa.			The maximum UTS was achieved from Zn-0.27wt%Y at 219MPa, comparing to the pure Zn at 62 MPa.		
Degradation rate	Hank's solution, 15 days			SBF, 28 days		
	Increased	Decreased	Similar to Mg	Increased	Decreased	Similar to Zn
	Sm, Ce, Y, Eu, Tm, Lu, Dy, Ho	Gd, La	Sc, Pr, Sm, Nd (3 wt.%)	Lu, Er, Tm	Pr, Nd, Eu, Gd, La, Dy, Tb, Yb, Sm, Ho, Sc	Ce, Y
	The corrosion resistance of Mg-light REE alloys was generally better than the pure Mg.			The corrosion rate of the alloy was maintained at 80–110 $\mu m/y$.		
In vitro biocompatibility	Cytotoxicity	Hemolysis rates		Cytotoxicity	Hemolysis rates	
	MC3T3-E1: 3 days, >90% of control	Mg-RE (Pr, Nd, Sm, Eu, Gd, Dy, Ho, and Yb) < pure Mg		MC3T3-E1: 3 days >90% of control	Zn-RE (Sc, Y, La, Ce, Pr, Nd, Eu, Gd, Tb, Ho, Er, Lu) < pure Zn	
In vivo biocompatibility ⁶⁷	Mg-RE alloy (wt%)	Implant site	Result	Zn-RE alloy (wt%)	Implant site	Result
	Mg-0.69La Mg-1.27Ce Mg-2.13Nd	Bone tissue of rabbits, 4weeks	No toxicological effects	Zn-0.42La Zn-0.43Ce Zn-0.44Nd	Tibia of rabbits; 6 & 12weeks	Enhanced osseointegration ability

Fig. 8. Comparison of the REE effects on biodegradable Mg and Zn alloys.

4.2.3. Biodegradation behaviors

Generally comparing the biodegradation rate of the Zn-RE and Mg-RE alloys, most of the Zn-RE alloys exhibit slower degradation rates than Zn, while most of the Mg-RE alloys present elevated degradation rates, especially the Mg-RE alloys with high concentrations of 10 wt% of REEs (Dy, Ho, Er, Tm, and Lu) showing one-order higher corrosion rates than the pure Mg. It is expected that alloying REEs to Zn and Mg would inhibit the corrosion rate as the corrosion products of REEs, oxides/hydroxides, are more compact and could incorporate into the corrosion product layer on the surfaces, which could protect the alloys from further corrosion [75]. The group of REEs including Tm, Er and Lu, increases the corrosion rate of Zn, while the group of REEs including Pr, Eu, Nd decreases that of Zn. As for the enhancement effect of REEs on the degradation rate of Mg alloy, the original literature also mentioned that the corrosion rates of some Mg-RE alloys increased with increasing REE content, including Mg-Sm, Mg-Ce, Mg-Y, Mg-Eu, Mg-Tm, Mg-Lu, Mg-Dy and Mg-Ho alloy systems. Taking Mg-Y alloy as an example, it is pointed out that with the increase of Y content, the grain size of the material increases and the amount of degradation of the material increases [38]. Since the rapid corrosion of the Mg has been an issue for its biomedical applications, the inhibited corrosion behaviors of low concentration alloyed Mg-RE alloys, especially Mg-1RE (Pr, Sm, Ce, and Sc) could be further developed for more biomedical applications. The corrosion rates of Zn-RE alloys are much lower than those of Mg-RE alloys and vary within a relatively narrow range probably due to low amount of REEs addition, suggesting substantial potential in biomedical field.

4.2.4. Biocompatibility

The *in vitro* cell assessment results show that the cell viabilities of the MC3T3-E1 cells from the Mg-RE alloys extracts are generally higher than those of MC3T3-E1 cells from Zn-RE alloys extracts as the degradation rate of Mg-RE alloys was high and the extracts were not diluted [38]. This is mainly attribute to the fact that Mg is one of the essential macro-elements in the human body despite of the deteriorating factor of high pH resulted from Mg-RE alloy degradation, while Zn is an essential trace element. However, the effect of the REEs' addition to Zn seems not very significant (117%~103% for Zn-RE alloys vs. 110% for pure Zn for 1 day), while the addition of the REEs varied the cytocompatibility of the Mg in a more intensive extent (124%~95% for Mg-RE alloys vs. 106% for pure Mg for 1 day) [38]. With the cell culture time prolonged to 3 days, the cell viabilities of most Mg-RE alloys decreased and only four REEs exhibited higher viability than pure Mg. For the Zn-RE alloys, there is a tendency that the cytocompatibilities of the Zn-RE alloys is better than that of pure Zn along the culture time extended to 3 days and 5 days. It has been reported that the initial inhibitory concentration of light rare earth elements (La to Pr) on different cells including human osteosarcoma cell line MG63, human umbilical cord perivascular (HUCPV) cells and mouse macrophages (RAW 264.7), was 30–600 μM compared to that of most medium and heavy rare earth elements (Nd, Sm to Lu) was about 2000 μM [37]. The concentration of RE3+ in the material extract was not out of the limit of detection of ICP-OES, suggesting that the released RE3+ was much lower than the initial inhibition concentration of cells. So it could be explained from the low concentration of the REEs and the recovery of mitochondrial damage caused by metal extractions. There are some common elements that decrease the cytocompatibility of both Zn and Mg, including Yb, Gd and Dy.

In terms of the *in vitro* hemocompatibility, all the Zn-RE alloys present excellent hemolysis rate lower than 5%. Similarly, most of Mg-RE alloys showed great hemolysis rate below 5%, except Mg-1Lu and Mg-10Lu alloys with the hemolysis rate of 10% and 95%, respectively [38]. The hemolysis rates of Mg-RE (Pr, Nd, Sm, Eu, Gd, Dy, Ho, Yb) alloy groups showed a decreasing trend. However, the hemolysis rate of three Mg-RE (Sm, Dy, Yb) alloys increased with the increase of alloying element content, which was higher than that of the pure Mg control

group [38]. As shown in Fig. 4(e), the addition of elements Sc, Y, La, Ce, Pr, Nd, Eu, Gd, Tb, Ho, Er, Lu into Zn were all able to reduce the hemolysis rate compared to the pure Zn control. Neither Mg-RE nor Zn-RE alloy groups produced significant adhesion and spreading of platelets on the material surface. By comparing the effect of REEs on the hemolysis rate of the two alloys, it can be found that a small amount of most REEs added to Zn can reduce the hemolysis rate. Even the Zn-Yb alloy group with the highest hemolysis rate, but did not exceed 5%. But the addition of half of the REEs to Mg can increase the hemolysis rate. Based on the comparison of the above data, it can be found that the addition of REEs into Zn as alloying elements has less interference on cells or blood. The effect of REEs' addition on the cell metabolism should also be concerned for both Zn-RE and Mg-RE alloys as a more in-depth investigation on the REEs' cytocompatibility would be helpful to assess chronic toxicity and immunotoxicity to organisms for biodegradable Zn-RE and Mg-RE alloys.

The *in vivo* implantation of the Zn-RE and Mg-RE alloys were conducted to evaluate the *in vivo* biocompatibility, and the capability of Zn-RE alloys to assist bone formation. Our work can compare to the work from Witte et al. [67]. Three alloys, Zn/Mg-La, Zn/Mg-Ce and Zn/Mg-Nd, were correspondingly conducted using New Zealand white rabbit model in tibia and knee joint respectively. The weight concentration of the REEs in Mg were 1.27 wt%, 0.69 wt% and 2.13 wt%, roughly comparable to the Zn-RE alloys. All the Zn-RE alloys showed the excellent systemic biocompatibility without any adverse reactions to blood, tissues and organs in 12 weeks period. Compared to the pure Zn implant, an enhanced osseointegration from the Zn-RE alloy implants can be observed and there was no significant volume loss occurred after 12 weeks of implantation, suggesting that the slow degradation rate of the Zn-RE alloys enables the mechanical integrity to be an ideal bone implant for longer implantation time. In the case of the Mg-RE alloys, there was no clinically health problems caused to the animal, although the *in vivo* degradation was observed for all Mg-RE alloys after 4 weeks, i.e., 81.75%, 86.54% and 80.61% of the Mg-La, Mg-Nd and Mg-Ce implant were presented respectively. In addition, no enhanced bone formation in the vicinity of Mg-RE implants were found. More Zn/Mg-RE alloys could be tested using animal models to generate more insights for researchers to evaluate, compare and improve the biodegradable metallic materials with REEs.

4.3. Prospective on Zn-RE alloys

Biodegradable metals and alloys are mainly developed and adopted for cardiovascular stents, bone scaffolds, bone screws and bone plates for tissue repair. The comparisons between the Zn-RE alloys and other Zn alloys, and Mg-RE alloys suggest huge potentials of the Zn-RE alloys in biomedical implants and devices.

4.3.1. Cardiovascular stents and bone scaffolds using Zn-RE alloys

The general design criteria for a biodegradable metal stent are summarized by Drynda et al. [76], requiring the nontoxic, non-inflammatory and hypoallergenic materials, and TYS >200 MPa, UTS >300 MPa and $\delta > 15\%$, and corrosion rate <20 $\mu\text{m}/\text{y}$, and mechanical integrity for 3–6 months and full degradation in 12–24 months. Similarly, for bone fixation applications, the implant materials are required to possess TYS >200 MPa and $\delta > 15\%$, degradation rate <0.5 mm/y, and maintain a service life of 3–6 months [77].

From our investigation, all the Zn-RE alloys exhibit outstanding hemocompatibility and cytocompatibility especially to human umbilical vein endothelial cells, suggesting biocompatible enough as the stent materials and bone scaffolds, screws and plates. Furthermore, the detailed cytocompatibility of Ce, Nd, Y and Yb to human vascular smooth muscle cells was assessed and these REEs did not lead to significant changes in metabolic activity and only induced upregulation of inflammatory genes at very high concentration of 50 mg/L [78]. Other REEs present the capability of bone-enabling, like La in the form of

released ion can promote the expression of relevant osteogenic genes through Wnt/ β -catenin signaling pathway [79], Y can promote osteogenic differentiation [80], while La, Sm, and Er inhibit osteoclastogenesis at low concentrations [81]. For the applications of Zn-RE alloys as the implant materials for cardiovascular stents and bone scaffolds, the biocompatibility is sufficiently acceptable with additional benefits.

Although the degradation rates of the Zn-RE alloys is much higher than the required rate for stent and lower than that for bone scaffolds applications, the degradation behaviors of the degradable metals are highly dependent on the micro-environment [11,13], especially, the *in vivo* degradation process is usually much complicated and commonly slower than the *in vitro* assessment. The implantation of the three Zn-RE alloys into the New Zealand rabbit model demonstrated well-maintained morphology of the implants within 12 weeks without observable mass loss. This could be the case when Zn-RE alloys are used in the cardiovascular environment as the stent. It further exhibits the great mechanical integrity of the Zn-RE alloys to play the role of mechanical supporting as the implants even though the TYS of these Zn-RE alloys is 13.5% lower than the criterion. Therefore, it is possible to category the Zn-RE alloys, mainly Zn–Y, Ho, Lu, as the most suitable candidates for stents and bone scaffolds, and the Zn-RE alloys, including Zn–Sc, La, Ce, Pr, Nd, Sm, La, as potential candidates.

To further improve the properties of the Zn-RE alloys, the future work can be focused on the alloy composition variation in alloy elements type and quantity, more comprehensive assessments with cells on inflammatory and gene regulations, and the REEs effects on the biocompatibility together with Zn. The first possible option is to have combinations of two or more of the best REEs candidates, Y, Ho and Lu. However, the single-phased solid solution with both solid-solution strengthening and grain refinement strengthen effects can be expected for improved mechanical strength. Also the addition of other alloying elements for mechanical strengthening can be considered, for example, Li, Cu, Mg or Mn according to previous reported dramatic enhancement in mechanical properties and varied corrosion rates [24,27].

4.3.2. Therapeutic effect of Zn-RE alloys

Due to the special radius which close to Ca^{2+} (main components of bone tissue) and higher charge number, RE ions have a higher affinity for Ca^{2+} sites on biomolecules and hence can act as either Ca^{2+} inhibitors or probes [82]. A current application for lanthanum carbonate (Fosrenol) as a phosphate binder for treatment of hyperphosphatemia in renal dialysis patients has been approved in both USA and Europe and available in market now [83]. RE ions and their compounds have also been investigated for their anti-cancer potential. For example, Gd^{3+} and Nd^{3+} can promote apoptosis of MG63 human osteosarcoma cells [37], Nd^{3+} was able to facilitate the synthesis of antitumor factors [84], Sm^{3+} and Eu^{3+} also showed anti-tumor effects [85], La^{3+} was demonstrated the inhibition effect on the proliferation and migration activities of human cervical cancer cells and induced their apoptosis [86]. The reversible conversion of Ce^{3+} and Ce^{4+} can cause oxidative stress by producing of reactive oxygen species (ROS) which can attack biomolecules such as nucleic acids, proteins, polysaccharides, and lipids [87]. Most of the above studies have investigated the effect of REEs on tumor inhibition from a molecular perspective, and no animal implantation experiments have been performed. Therefore, Gd, Nd, Eu, and La elements could be the targeted REEs in the Zn-RE alloys for the development of functionalized implantable devices with bone tumor inhibition.

5. Conclusions

In this work, 16 REEs in 0.2 at% were respectively alloyed into pure Zn to regulate the comprehensive properties of pure Zn. The pure Zn and all the Zn-0.2 at%RE alloys were processed under the same deformation conditions. The microstructure, mechanical properties, corrosion behavior, *in vitro* and *in vivo* biocompatibility were investigated

symmetrically. The conclusions are drawn as below.

- (1) Alloying REEs improves TYS, UTS, and UE of Zn. The improvement effects of each REE on the microstructure and mechanical properties of Zn are different. Y increases tensile strength and hardness most, while both Ho and Lu enhance the plasticity most obviously.
- (2) The addition of REEs can adjust the corrosion rate of Zn. The corrosion rate of Zn–Y, Zn–Lu, Zn–Er and Zn–Tm is higher than that of pure Zn. There are four Zn-RE alloys, including Zn–Pr, Zn–Nd, Zn–Eu and Zn–Gd, that corrode slower than pure Zn. ZnO, carbonate and phosphate are the main corrosion products for all the Zn-RE alloys.
- (3) The excellent *in vitro* biocompatibility including cytocompatibility and hemocompatibility are achieved for most of the Zn-RE alloys. Three alloys, Zn–La, Zn–Ce and Zn–Nd, exhibit superior *in vivo* biocompatibility and the improved osseointegration in the animal tibia model compared to that of the pure Zn. Diffusion of REEs around bone tissue was observed in hard tissue sections, suggesting the *in vivo* degradation of Zn-RE alloys.
- (4) Among the 16 Zn-RE alloys, we found that the Y, Ho and Lu were the best alloying elements for Zn with superior mechanical properties, biodegradation rate and biocompatibility. On the other hand, Eu, Dy and Gd were the three elements exhibiting not improved or worse performances among the REEs or compared to pure Zn.
- (5) To further improve the properties of the Zn-RE alloys, the future work can be focused on the alloy composition variation in alloy elements type and quantity, more comprehensive assessments with cells on inflammatory and gene regulations, and the REEs effects on the biocompatibility together with Zn. This work also will lead broader and more profound research both in materials science and biology and biomedical engineering fields towards practical applications.

Ethics approval

Animal experiment was approved by the Ethics Committee of Peking University Health Science Centre, Beijing, China (LA2019019). The surgery was carried out according to the protocol established by the Experimental Animal Ethics branch.

CRediT authorship contribution statement

Shaokang Du: Data curation, Formal analysis, Investigation, Methodology, Validation, Writing – original draft. **Yunong Shen:** Data curation, Formal analysis, Investigation, Methodology. **Yufeng Zheng:** Conceptualization, Funding acquisition, Project administration, Resources, Supervision, Writing – review & editing. **Yan Cheng:** Conceptualization, Methodology, Supervision, Resources. **Xiaoxue Xu:** Conceptualization, Methodology, Supervision, Writing – review & editing. **Dafu Chen:** Methodology, Resources, Supervision. **Dandan Xia:** Methodology, Supervision, Validation, Review & Editing, Writing – review & editing.

Declaration of competing interest

The authors declared that they have no conflicts of interest to this paper. We declare that we do not have any commercial or associative interest that represents a conflict of interest in connection with this paper.

Acknowledgments

This work was supported by the National Key R&D Program of China [2018YFE0104200]; the National Natural Science Foundation of China

[51931001, 52171233, 52271243, U22A20121]; the INTERNATIONAL COOPERATION and Exchange project of NSFC-RFBR [52111530042]; the Beijing Natural Science Foundation [L212014]; and the Beijing Nova Program.

Appendix A. Supplementary data

Supplementary data to this article can be found online at <https://doi.org/10.1016/j.bioactmat.2023.01.004>.

References

- [1] Y.F. Zheng, X.N. Gu, F. Witte, Biodegradable metals, *Mater. Sci. Eng. R Rep.* (77) (2014) 1–34.
- [2] Y. Liu, Y.F. Zheng, X.H. Chen, J.A. Yang, H.B. Pan, D.F. Chen, L.N. Wang, J. L. Zhang, D.H. Zhu, S.L. Wu, K.W.K. Yeung, R.C. Zeng, Y. Han, S.K. Guan, Fundamental theory of biodegradable metals-definition, criteria, and design, *Adv. Funct. Mater.* 29 (18) (2019).
- [3] W. Lin, L. Qin, H. Qi, D. Zhang, G. Zhang, R. Gao, H. Qiu, Y. Xia, P. Cao, X. Wang, Long-term in vivo corrosion behavior, biocompatibility and bioresorption mechanism of a bioresorbable nitrided iron scaffold, *Acta Biomater.* 54 (2017) 454–468.
- [4] M. Peuster, C. Hesse, T. Schloo, C. Fink, P. Beerbaum, C.V. Schnakenburg, Long-term biocompatibility of a corrodible peripheral iron stent in the porcine descending aorta, *Biomaterials* 27 (28) (2006) 4955–4962.
- [5] D. Bian, J. Deng, N. Li, X. Chu, Y. Liu, W. Li, H. Cai, P. Xiu, Y. Zhang, Z. Guan, In vitro and in vivo studies on biomedical magnesium low-alloying with elements gadolinium and zinc for orthopedic implant applications, *ACS Appl. Mater. Interfaces* 10 (5) (2018) 4394–4408.
- [6] Jian Zhang, Haiyan Li, Wu Wang, Hua Huang, Jia Pei, The degradation and transport mechanism of a Mg-Nd-Zn-Zr stent in rabbit common carotid artery: a 20-month study, *Acta Biomater.* 69 (2018) 372–384.
- [7] N. Hort, Y. Huang, D. Fechner, M. Störmer, C. Blawert, F. Witte, C. Vogt, H. Drücker, R. Willumeit, K.U. Kainer, Magnesium alloys as implant materials—principles of property design for Mg-RE alloys, *Acta Biomater.* 6 (5) (2010) 1714–1725.
- [8] H. Li, H. Yang, Y. Zheng, F. Zhou, K. Qiu, W. Xiang, Design and characterizations of novel biodegradable ternary Zn-based alloys with IIA nutrient alloying elements Mg, Ca and Sr, *Mater. Des.* 83 (15) (2015) 95–102.
- [9] Y. Xin, T. Hu, P.K. Chu, In vitro studies of biomedical magnesium alloys in a simulated physiological environment: a review, *Acta Biomater.* 7 (4) (2011) 1452–1459.
- [10] D. Vojtěch, J. Kubásek, J. Šerák, P. Novák, Mechanical and corrosion properties of newly developed biodegradable Zn-based alloys for bone fixation, *Acta Biomater.* 7 (9) (2011) 3515–3522.
- [11] H. Yang, C. Wang, C. Liu, H. Chen, Y. Wu, J. Han, Z. Jia, W. Lin, D. Zhang, W. Li, Evolution of the degradation mechanism of pure zinc stent in the one-year study of rabbit abdominal aorta model, *Biomaterials* 145 (2017) 92–105.
- [12] J. Ma, N. Zhao, D. Zhu, Endothelial cellular responses to biodegradable metal zinc, *ACS Biomater. Sci. Eng.* 1 (11) (2015) 1174–1182.
- [13] Hongtao Yang, Xinhua Qu, Wenjiao Lin, Cong Wang, Donghui Zhu, In vitro and in vivo studies on zinc-hydroxyapatite composites as novel biodegradable metal matrix composite for orthopedic applications, *Acta Biomater.* 71 (2018) 200–214.
- [14] Bing-Li Bai, Zhou Qiang, Hang Li, Yang-Xun Lv, Zheng-Liang Huang, A comparative study of zinc, magnesium, strontium-incorporated hydroxyapatite-coated titanium implants for osseointegration of osteopenic rats, *Mater. Sci. Eng. C Mater. Bio. Appl.* 62 (2016) 226–232.
- [15] J.P. O'Connor, D. Kanjilal, M. Teitelbaum, S.S. Lin, J.A. Cottrell, Zinc as a therapeutic agent in bone regeneration, *Materials* 13 (10) (2020) 1–22.
- [16] A. Kafri, S. Ovadia, G. Yosafovich-Doitch, E. Aghion, In vivo performances of pure Zn and Zn-Fe alloy as biodegradable implants, *J. Mater. Sci. Mater. Med.* 29 (7) (2018).
- [17] K. Alon, O. Shira, G. Jeremy, D. Jaroslaw, A. Eli, The suitability of Zn–1.3%Fe alloy as a biodegradable implant material, *Metal. Open Acc. Metal. J.* 8 (3) (2018) 153.
- [18] M.S. Dambatta, S. Izman, H. Hermawan, D. Kurniawan, Influence of heat treatment cooling mediums on the degradation property of biodegradable Zn-3Mg alloy, *Adv. Mater. Res.* 845 (2014) 7–11.
- [19] M.S. Dambatta, S.K. Yeap, G. Froemming, H. Hermawan, Cytotoxicity evaluation of biodegradable Zn–3Mg alloy toward normal human osteoblast cells, *Mater. Sci. Eng. C* 49 (2015) 560–566.
- [20] Y. Zou, X. Chen, B. Chen, Effects of Ca concentration on degradation behavior of Zn-x Ca alloys in Hank's solution, *Mater. Lett.* 218 (MAY1) (2018) 193–196.
- [21] Y. Su, J. Fu, S. Du, E. Georgas, Y.-X. Qin, Y. Zheng, Y. Wang, DonghuiZhu, Biodegradable Zn–Sr alloys with enhanced mechanical and biocompatibility for biomedical applications, *Smart Mater. Med.* 3 (2022) 117–127.
- [22] B. Jia, H. Yang, Z. Zhang, X. Qu, X. Jia, Q. Wu, Y. Han, Y. Zheng, K. Dai, Biodegradable Zn-Sr alloy for bone regeneration in rat femoral condyle defect model: in vitro and in vivo studies, *Bioact. Mater.* 6 (6) (2021) 1588–1604.
- [23] Li Zhen, Shi Zhang-Zhi, Hao Yuan, Li Hua-Fang, Liu Xue-Feng, High-performance hot-warm rolled Zn-0.8Li alloy with nano-sized metastable precipitates and sub-micron grains for biodegradable stents, *J. Mater. Sci. Technol.* 35 (11) (2019) 2618–2624.
- [24] S. Zhao, C.T. McNamara, P.K. Bowen, N. Verhun, J.P. Braykovich, J. Goldman, J. W. Drelich, Structural characteristics and in vitro biodegradation of a novel Zn-Li alloy prepared by induction melting and hot rolling, *Metall. Mater. Trans.* 48 (3) (2017) 1204–1215.
- [25] X. Qu, H. Yang, B. Jia, Z. Yu, Y. Zheng, K. Dai, Biodegradable Zn–Cu alloys show antibacterial activity against MRSA bone infection by inhibiting pathogen adhesion and biofilm formation, *Acta Biomater.* 117 (2020) 400–417.
- [26] Y. Xie, L. Zhao, Z. Zhe, X. Wang, C. Cui, Fabrication and properties of porous Zn-Ag alloy scaffolds as biodegradable materials, *Mater. Chem. Phys.* 219 (2018) 433–443.
- [27] H. Yang, B. Jia, Z. Zhang, X. Qu, G. Li, W. Lin, D. Zhu, K. Dai, Y. Zheng, Alloying design of biodegradable zinc as promising bone implants for load-bearing applications, *Nat. Commun.* 11 (1) (2020) 401.
- [28] S. Lin, Q. Wang, X. Yan, X. Ran, L. Wang, J.G. Zhou, T. Hu, G. Wang, Mechanical properties, degradation behaviors and biocompatibility evaluation of a biodegradable Zn-Mg-Cu alloy for cardiovascular implants, *Mater. Lett.* 234 (JAN.1) (2019) 294–297.
- [29] X. Liu, J. Sun, F. Zhou, Y. Yang, R. Chang, K. Qiu, Z. Pu, L. Li, Y. Zheng, Micro-alloying with Mn in Zn–Mg alloy for future biodegradable metals application, *Mater. Des.* 94 (2016) 95–104.
- [30] X. Shao, X. Wang, F. Xu, T. Dai, J.G. Zhou, J. Liu, K. Song, L. Tian, B. Liu, Y. Liu, In vivo biocompatibility and degradability of a Zn-Mg-Fe alloy osteosynthesis system, *Bioact. Mater.* (1) (2022) 154–166.
- [31] Z. Zhang, B. Jia, H. Yang, Y. Han, Q. Wu, K. Dai, Y. Zheng, Biodegradable ZnLiCa ternary alloys for critical-sized bone defect regeneration at load-bearing sites: In vitro and in vivo studies, *Bioact. Mater.* 6 (11) (2021) 15.
- [32] Z. Zhang, B. Jia, H. Yang, Y. Han, Q. Wu, K. Dai, Y. Zheng, Zn0.8Li0.1Sr—a biodegradable metal with high mechanical strength comparable to pure Ti for the treatment of osteoporotic bone fractures: in vitro and in vivo studies, *Biomaterials* 275 (3) (2021), 120905.
- [33] H. Amano, K. Miyake, A. Hinoki, K. Yokota, F. Kinoshita, A. Nakazawa, Y. Tanaka, Y. Seto, H. Uchida, Novel zinc alloys for biodegradable surgical staples, *World J. Clin. Case* 8 (3) (2020) 13.
- [34] S. Gavras, M.A. Easton, M.A. Gibson, S. Zhu, J.F. Nie, Microstructure and property evaluation of high-pressure die-cast Mg–La–rare earth (Nd, Y or Gd) alloys, *J. Alloys Compd.* 597 (2014) 21–29.
- [35] G. Song, A. Arens, Understanding magnesium corrosion—a framework for improved alloy performance, *Adv. Eng. Mater.* 5 (12) (2003) 837–858.
- [36] L.L. Rokhlin, Magnesium alloys containing rare-earth metals, in: *Structure and Properties* vol. 3, Crc Press, 2004, 10.
- [37] F. Feyerabend, J. Fischer, J. Holtz, F. Witte, R. Willumeit, H. Drücker, C. Vogt, N. Hort, Evaluation of short-term effects of rare earth and other elements used in magnesium alloys on primary cells and cell lines, *Acta Biomater.* 6 (5) (2010) 1834–1842.
- [38] J. Liu, D. Bian, Y. Zheng, X. Chu, Y. Lin, M. Wang, Z. Lin, M. Li, Y. Zhang, S. Guan, Comparative in vitro study on binary Mg-RE (Sc, Y, La, Ce, Pr, Nd, Sm, Eu, Gd, Tb, Dy, Ho, Er, Tm, Yb and Lu) alloy systems, *Acta Biomater.* (102) (2020) 508–528.
- [39] Z. Zhu, A.D. Pelton, Critical assessment and optimization of phase diagrams and thermodynamic properties of RE–Zn systems-part I: Sc–Zn, La–Zn, Ce–Zn, Pr–Zn, Nd–Zn, Pm–Zn and Sm–Zn, *J. Alloys Compd.* 641 (2015) 249–260.
- [40] Z. Zhu, A.D. Pelton, Critical assessment and optimization of phase diagrams and thermodynamic properties of RE–Zn systems – Part II – Y–Zn, Eu–Zn, Gd–Zn, Tb–Zn, Dy–Zn, Ho–Zn, Er–Zn, Tm–Zn, Yb–Zn and Lu–Zn, *J. Alloys Compd.* 641 (2015) 261–271.
- [41] A.S.f.T.a. Materials, ASTM-E8-04, Standard Test Methods for Tension Testing of Metallic Materials, annual book of ASTM standards, West Conshohocken, PA, 2004.
- [42] A.S.f.T.a. Materials, ASTM E9-89A. Standard Test Methods of Compression Testing of Metallic Materials at Room Temperature, 2000. West Conshohocken, PA.
- [43] A.S.f.T.a. Materials, ASTM G102-89, Standard Practice for Calculation of Corrosion Rates and Related Information from Electrochemical Measurements, American Society for Testing and Materials, 2010.
- [44] A.S.f.T.a. Materials, ASTM G31-72, Standard Practice for Laboratory Immersion Corrosion Testing of Metals, annual book of ASTM standards, West Conshohocken, PA, 2004.
- [45] A.S.f.T.a. Materials, ASTM G1-90, Standard Practice for Preparing, Cleaning, and Evaluating Corrosion Test Specimens, annual book of ASTM standards West, Conshohocken, PA, 1999.
- [46] T.a. Ko, S.L. Cooper, Surface properties and platelet adhesion characteristics of acrylic acid and allylamine plasma-treated polyethylene, *J. Appl. Polym. Sci.* 47 (9) (2010) 1601–1619.
- [47] Z.-Z. Shi, X.-X. Gao, H.-J. Zhang, X.-F. Liu, H.-Y. Li, C. Zhou, Y.-X. Yin, L.-N. Wang, Design biodegradable Zn alloys: second phases and their significant influences on alloy properties, *Bioact. Mater.* 5 (2) (2020) 210–218.
- [48] N. Takata, Y. Ohtake, K. Kita, K. Kitagawa, N. Tsuji, Increasing the ductility of ultrafine-grained copper alloy by introducing fine precipitates, *Scripta Mater.* 60 (7) (2009) 590–593.
- [49] C. Wang, H.T. Yang, X. Li, Y.F. Zheng, In vitro evaluation of the feasibility of commercial Zn alloys as biodegradable metals, *J. Mater. Sci. Technol.* 32 (9) (2016) 909–918.
- [50] Z. Tang, J. Niu, H. Huang, H. Zhang, J. Pei, J. Ou, G. Yuan, Potential biodegradable Zn-Cu binary alloys developed for cardiovascular implant applications, *J. Mech. Behav. Biomed. Mater.* 72 (2017) 182–191.
- [51] J. Kubásek, D. Vojtěch, E. Jablonská, I. Pospíšilová, J. Lipov, T. Ruml, Structure, mechanical characteristics and in vitro degradation, cytotoxicity, genotoxicity and

- mutagenicity of novel biodegradable Zn–Mg alloys, *Mater. Sci. Eng. C* 58 (2016) 24–35.
- [52] M. Sikora-Jasinska, E. Mostaed, A. Mostaed, R. Beanland, D. Mantovani, M. Vedani, Fabrication, mechanical properties and in vitro degradation behavior of newly developed ZnAg alloys for degradable implant applications, *Mater. Sci. Eng. C* 77 (2017) 1170–1181.
- [53] J.J. Gao, L. Feng, B.L. Chen, B. Fu, M. Zhu, The role of rare earth elements in bone tissue engineering scaffolds—A review, *Compos. B Eng.* 235 (2022) 15.
- [54] P. Li, W. Zhang, J. Dai, A.B. Xepapadeas, E. Schweizer, D. Alexander, L. Scheideler, C. Zhou, H. Zhang, G. Wan, J. Geis-Gerstorfer, Investigation of zinc-copper alloys as potential materials for craniomaxillofacial osteosynthesis implants, *Mater. Sci. Eng. C* 103 (2019), 109826.
- [55] H. Li, H. Yang, Y. Zheng, F. Zhou, K. Qiu, X. Wang, Design and characterizations of novel biodegradable ternary Zn-based alloys with IIA nutrient alloying elements Mg, Ca and Sr, *Mater. Des.* 83 (2015) 95–102.
- [56] X. Liu, J. Sun, K. Qiu, Y. Yang, Z. Pu, L. Li, Y. Zheng, Effects of alloying elements (Ca and Sr) on microstructure, mechanical property and in vitro corrosion behavior of biodegradable Zn–1.5Mg alloy, *J. Alloys Compd.* 664 (2016) 444–452.
- [57] G.J. Fosmire, Zinc toxicity, *Am. J. Clin. Nutr.* 51 (2) (1990) 225–227.
- [58] Z. Li, Z.-Z. Shi, Y. Hao, H.-F. Li, H.-J. Zhang, X.-F. Liu, L.-N. Wang, Insight into role and mechanism of Li on the key aspects of biodegradable ZnLi alloys: microstructure evolution, mechanical properties, corrosion behavior and cytotoxicity, *Mater. Sci. Eng. C* 114 (2020), 111049.
- [59] X. Wang, X. Shao, T. Dai, F. Xu, J.G. Zhou, G. Qu, L. Tian, B. Liu, Y. Liu, In vivo study of the efficacy, biosafety, and degradation of a zinc alloy osteosynthesis system, *Acta Biomater.* 92 (2019) 351–361.
- [60] G. Katarivas Levy, J. Goldman, E. Aghion, The prospects of zinc as a structural material for biodegradable implants—a review paper, *Metals* 7 (10) (2017).
- [61] H. Jin, S. Zhao, R. Guillory, P.K. Bowen, Z. Yin, A. Griebel, J. Schaffer, E.J. Earley, J. Goldman, J.W. Drelich, Novel high-strength, low-alloys Zn–Mg (<0.1wt% Mg) and their arterial biodegradation, *Mater. Sci. Eng. C* 84 (2018) 67–79.
- [62] S.V. Eliseeva, J.-C.G. Bünzli, Lanthanide luminescence for functional materials and bio-sciences, *Chem. Soc. Rev.* 39 (1) (2010) 189–227.
- [63] Y. Huang, X. Zhai, T. Ma, M. Zhang, H. Pan, W. Weijia Lu, X. Zhao, T. Sun, Y. Li, J. Shen, C. Yan, Y. Du, Rare earth-based materials for bone regeneration: breakthroughs and advantages, *Coord. Chem. Rev.* 450 (2022), 214236.
- [64] H. Naujokat, A. Gülses, J. Wiltfang, Y. Açil, Effects of degradable osteosynthesis plates of MgYREZr alloy on cell function of human osteoblasts, fibroblasts and osteosarcoma cells, *J. Mater. Sci. Mater. Med.* 28 (8) (2017) 1–9.
- [65] Y. Liu, Y. Lin, D. Bian, M. Wang, Z. Lin, X. Chu, W. Li, Y. Liu, Z. Shen, Y. Liu, Y. Tong, Z. Xu, Y. Zhang, Y. Zheng, In vitro and in vivo studies of Mg–30Sc alloys with different phase structure for potential usage within bone, *Acta Biomater.* 98 (2019) 50–66.
- [66] L. Yang, Y. Huang, F. Feyerabend, R. Willumeit, K.U. Kainer, N. Hort, Influence of ageing treatment on microstructure, mechanical and bio-corrosion properties of Mg–Dy alloys, *J. Mech. Behav. Biomed. Mater.* 13 (2012) 36–44.
- [67] E. Willbold, X. Gu, D. Albert, K. Kalla, K. Bobe, M. Brauneis, C. Janning, J. Nellesen, W. Czayka, W. Tillmann, Effect of the addition of low rare earth elements (lanthanum, neodymium, cerium) on the biodegradation and biocompatibility of magnesium, *Acta Biomater.* 11 (2015) 554–562.
- [68] K. Yu, Y. Dai, Z. Luo, H. Long, M. Zeng, Z. Li, J. Zhu, L. Cheng, Y. Zhang, H. Liu, Y. Zhu, In vitro and in vivo evaluation of novel biodegradable Mg–Ag–Y alloys for use as resorbable bone fixation implant, *J. Biomed. Mater. Res., Part A* 106 (7) (2018) 2059–2069.
- [69] K. Munir, J. Lin, C. Wen, P.F.A. Wright, Y. Li, Mechanical, corrosion, and biocompatibility properties of Mg–Zr–Sr–Sc alloys for biodegradable implant applications, *Acta Biomater.* 102 (2020) 493–507.
- [70] Y. Ding, J. Lin, C. Wen, D. Zhang, Y. Li, Mechanical properties, in vitro corrosion and biocompatibility of newly developed biodegradable Mg–Zr–Sr–Ho alloys for biomedical applications, *Sci. Rep.* 6 (1) (2016), 31990–31990.
- [71] X. Zhang, G. Yuan, J. Niu, P. Fu, W. Ding, Microstructure, mechanical properties, biocorrosion behavior, and cytotoxicity of as-extruded Mg–Nd–Zn–Zr alloy with different extrusion ratios, *J. Mech. Behav. Biomed. Mater.* 9 (2012) 153–162.
- [72] L. Liu, F. Yuan, M. Zhao, C. Gao, P. Feng, Y. Yang, S. Yang, C. Shuai, Rare earth element yttrium modified Mg–Al–Zn alloy: microstructure, degradation properties and hardness, *Materials* 10 (2017) 477–488.
- [73] G.Y. Yuan, X.B. Zhang, J.L. Niu, H.R. Tao, D.Y. Chen, H.E. Yao-Hua, Y. Jiang, W. J. Ding, Research progress of new type of degradable biomedical magnesium alloys JDBM, *Chin. J. Nonferrous Metals* 21 (10) (2011) 2476–2488.
- [74] Y. Li, C. Wen, T. Xian, D. Zhang, M. Dargusch, Development of biodegradable Zn–1Mg–0.1RE (RE=Er, Dy, and Ho) alloys for biomedical applications, *Acta Biomater.* 117 (2020) 384–399.
- [75] W. Liu, F. Cao, L. Chang, Z. Zhang, J. Zhang, Effect of rare earth element Ce and La on corrosion behavior of AM60 magnesium alloy, *Corrosion Sci.* 51 (6) (2009) 1334–1343.
- [76] P.K. Bowen, J. Drelich, J. Goldman, Zinc exhibits ideal physiological corrosion behavior for bioabsorbable stents, *Adv. Mater.* 25 (18) (2013) 2577–2582.
- [77] J. Yin, J. Yu, Q. Ke, Q. Yang, D. Zhu, Y. Gao, Y. Guo, C. Zhang, La-Doped biomimetic scaffolds facilitate bone remodelling by synchronizing osteointegration and phagocytic activity of macrophages, *J. Mater. Chem. B* 7 (19) (2019) 3066–3074.
- [78] A. Drynda, N. Deinet, N. Braun, M. Peuster, Rare earth metals used in biodegradable magnesium-based stents do not interfere with proliferation of smooth muscle cells but do induce the upregulation of inflammatory genes, *J. Biomed. Mater. Res.* 91A (2) (2010) 360–369.
- [79] X.Y. Peng, M. Hu, F. Liao, F. Yang, Q.F. Ke, Y.P. Guo, Z.H. Zhu, La-Doped mesoporous calcium silicate/chitosan scaffolds for bone tissue engineering, *Biomater. Sci.* 7 (4) (2019) 1565–1573.
- [80] X. Song, Y. Wu, D. Pan, J. Zhang, S. Xu, L. Gao, R. Wei, Z. Jin, G. Xiao, Dual-linker metal-organic frameworks as efficient carbon dioxide conversion catalysts, *Appl. Catal. Gen.* 566 (2018) 44–51.
- [81] J. Zhang, X.U. Shanjin1, W. Kui, Y. Shifeng, Effects of the rare earth ions on bone resorbing function of rabbit mature osteoclasts in vitro, *Chin. Sci. Bull.* 48 (20) (2003) 2170–2175.
- [82] A. Palasz, P. Czekaj, Toxicological and cytophysiological aspects of lanthanides action, *Acta Biochim. Pol.* 47 (4) (2000) 1107–1114.
- [83] H. Kawanishi, M. Ishida, M. Ishizaki, Y. Takuma, H. Tamura, S. Kobayashi, T. Tamura, H. Ohashi, M. Hiramatsu, J. Minakuchi, H. Hirakata, T. Shigematsu, Lanthanum carbonate treatment of patients with hyperphosphatemia undergoing CAPD, *Perit. Dial. Int.* 28 (6) (2008) 673–675.
- [84] M. Ali, M.A. Hussein, N. Al-Aqeeli, Magnesium-based composites and alloys for medical applications: a review of mechanical and corrosion properties, *J. Alloys Compd.* 792 (2019) 1162–1190.
- [85] C. Feng, Q. Gan, X. Liu, H. He, Synthesis, antitumor and apoptosis inducing activities of novel 5-fluorouracil derivatives of rare earth (Sm, Eu) substituted polyoxometalates, *Chin. J. Chem.* 30 (7) (2012) 5.
- [86] S.S. Liu, D. Lu, L.F. Miao, Q.Y. Xiong, X.P. Chen, Y. Wang, F. Guo, Effects of lanthanum chloride on proliferation and migration of human cervical cancer cell line HeLa cells, *Zhonghua Fu Chan Ke Za Zhi* 45 (8) (2010) 609–613.
- [87] Y. Lin, Z. Yang, J. Cheng, Preparation, characterization and antibacterial property of cerium substituted hydroxyapatite nanoparticles, *J. Rare Earths* 25 (4) (2007) 452–456.